Mechano-metabolism of adherent cells in 2D and 3D microenvironments

Anuja Jaganathan[1,2#], Joshua Toth[1,2#], Xingyu Chen[1,2], Laurent Pieuchot[3], Yihui Shen[4], Cynthia Reinhart-King[5], Vivek B. Shenoy[1,2,4,6*]

[1]Center for Engineering Mechanobiology, University of Pennsylvania, PA, US

[2]Department of Materials Science and Engineering, University of Pennsylvania, PA, US

[3]Université de Haute-Alsace, CNRS, IS2M UMR 7361, Mulhouse 68100, France

[4]Department of Bioengineering, University of Pennsylvania, PA, US

[5]Department of Biomedical Engineering, Vanderbilt University, Nashville, TN 37235, US

[6]Department of Mechanical Engineering and Applied Mathematics, University of Pennsylvania, PA, US

[#]Equal Contribution
*Correspondence to: vshenoy@seas.upenn.edu

Abstract

Cells regulate their shape and metabolic activity in response to the mechano-chemical properties of their microenvironment. To elucidate the impact of matrix stiffness and ligand density on a cell's bioenergetics, we developed a non-equilibrium, active chemo-mechanical model that accounts for mechanical energy of the cell and matrix, chemical energy from ATP hydrolysis, interfacial energy, and mechano-sensitive regulation of stress fiber assembly through signaling. By integrating the kinetics and energetics of these processes we introduce the concept of the metabolic potential of the cell that, when minimized, gives experimentally testable predictions of the cell contractility, shape, and the ATP consumption. Specifically, we show that MDA-MB-231 breast cancer cells in 3D collagen gels follow a spherical to spindle to spherical change in morphology with increasing matrix stiffness consistent with experimental observations. This biphasic transition in cell shape emerges from a competition between increased contractility accompanied by ATP hydrolysis enabled by mechano-sensitive signaling, which lowers the volumetric contribution to the metabolic potential of elongated cells and the interfacial energy which is lower for spherical shapes. On 2D hydrogels, our model predicts a hemispherical to spindle to disc shape transition with increasing gel stiffness. In both cases, we show that increasing matrix stiffness monotonically increases the cell's contractility as well as ATP consumption. Our model also predicts how the increased energy demand in stiffer microenvironments is met by AMPK activation, which is confirmed through experimental measurement of activated AMPK levels as a function of matrix stiffness carried out here in both 2D and 3D micro-environments. Further, model predictions of increased AMPK activation on stiffer micro-environments are found to correlate strongly with experimentally measured upregulation of mitochondrial potential, glucose uptake and ATP levels. The insights from our model can be used to understand mechanosensitive regulation of metabolism in physiological events such as metastasis and tumor progression during which cells experience dynamic changes in their microenvironment and metabolic state.

1 Introduction

It is established that cells feel and respond to their mechanical environment through reorganization of cytoskeletal architecture and control of actomyosin contractility[1]. Many studies link changes in contractility to changes in cell stiffness[2], cell shape[3], and cell differentiation[4,5] as the result of mechanosensitive biochemical pathways. It has also been shown that the cells' mechanical environment can regulate metabolic changes via a myriad of different mechanisms influencing, for example, cytoskeletal sequestering of glycolytic enzymes[6–9], lipid synthesis[10,11], mitochondria shape and function[12–14], and YAP/TAZ signaling[15,16]. However, the most immediate outcome impacting cellular energy availability in the context of a changing mechanical environment is the upregulation of adenosine triphosphate (ATP) production in response to increasing environmental stiffness through activation of the master metabolic regulator 5' adenosine monophosphate-activated protein kinase (AMPK)[14,17,18]. As a sensor of intracellular energy levels, regulation of the activity of this kinase affects several downstream pathways responsible for controlling the extent to which metabolic processes such as glucose uptake[19,20], glycolysis[21,22], oxidative phosphorylation (OXPHOS)[23], protein synthesis[24], and autophagy[25] occur. Thus, there is a clear connection between the energy-intensive processes involved in generation and maintenance of cell contractility and the need for AMPK to regulate the availability of energy within a contractile cell. Mechano-transduction and its role in regulating metabolism has physiological relevance, particularly in determining cancer cell migration, tumor progression and metastasis[26,27], with cancer cells reprogramming their metabolism in response to mechanical cues from the local micro-environment[28]. Studies investigating this interplay between forces transmitted from the ECM and cell metabolism in response to the mechanical microenvironment have been largely qualitative in nature. Therefore, predictive mathematical models that provide a unified framework to model the kinetics of mechano-signaling and the mechano-sensitive modulation of the energy available to cells stand to offer quantitative insight into the mechanisms governing the mechanosensitive nature of cell energetics and metabolism.

Here, we develop a chemo-mechanical model for contractility and adhesions based on the concept of a "metabolic potential" by explicitly accounting for the conversion of energy from ATP hydrolysis linked to myosin-II motor activity to both conservative chemical and mechanical energies associated with cell contractility and dissipative heat. We show that since these energies are modulated by mechanosensitive signaling pathways regulating myosin motor kinetics, cells will alter their contractility and morphology to *minimize their metabolic potential* in different microenvironments. We utilize this metabolic potential to make predictions regarding optimum cell shapes, contractility, and ATP consumption in environments with changing stiffness. Furthermore, we predict distinct differences in optimum cell shapes between cells on 2D substrates and cells in 3D matrices that arise purely because of variations in distribution of stresses generated as a consequence of the differences in the geometry that impact downstream chemo-mechanical signaling. Additionally, we introduce a theoretical framework for the replenishment of intracellular energy stores in response to upregulation of energy consuming processes such as stress fiber assembly by considering the parallel activation of AMPK. We show how, counterintuitively, intracellular ATP can be maintained at higher levels in highly contractile cells as a result of this homeostatic pathway. Our model makes testable predictions regarding cell morphology, contractility, and metabolic activity which we validate with experiments measuring cell shapes and intracellular ATP:ADP ratios in MDA-MB-231 cancer cells in environments of different stiffness. We find as well that measures of cell glucose uptake and mitochondria membrane potential correlate well with predicted AMPK activity. Our model thus provides a predictive quantitative tool for studying the interplay between mechanosensitive changes in cellular morphology, contractility, signaling and metabolism.

2 Materials and Methods

2.1 Mathematical description of a metabolic potential of adherent cells

In an adherent contractile cell, myosin-II motors bind to F-actin filaments and generate contractile forces, in the process, converting energy released through ATP hydrolysis into mechanical work[29,30]. Cell contraction generates tensile stresses in the cytoskeleton, particularly in stiffer microenvironments, which in turn can trigger mechanosensitive pathways such as the Rho-ROCK[31,32] and the Ca^{2+}/calmodulin pathways[33] (Figure 2a) that have the overall effect of upregulating the rate at which motors are recruited and the time for which they remain engaged (Figure S1). Therefore, the dynamic equilibrium of myosin motors is shifted towards the engaged state and the cells adopt a higher steady state level of contractility (higher density of engaged or "active" motors) in response to stiff microenvironments. Thus, stress-regulated mechano-signaling directly leads to higher levels of ATP consumption (in a time- averaged sense) on stiffer substrates.

We first formulate a metabolic potential for a cell held between two microposts[34] (Figure 1a) with the goal of predicting how the cytoskeletal contractility is modulated by the stiffness of the extracellular micro-environment and how the change in contractility is directly correlated to the amount of ATP consumed. This analysis lays the groundwork for the more general case of cells in 3D collagen networks and 2D gels. To capture the salient features of this mechano-sensitive metabolic regulation, we formulate an expression for the cell's metabolic potential as a function of cytoskeletal contractility and strain (Figure 2b) where the cell is considered an elastic element (representing the passive mechanical components of the cytoskeleton) in parallel with an active contractile element (representing stress fibers), while the microposts are modelled as elastic elements in series with the cell (Figure 1a). The myosin motors are modelled as force dipoles, and the contractile stress, or contractility, generated by engaged motors can be represented by the variable ρ (Figure S2). Note that the magnitude of ρ therefore also reflects the number density of active myosin motors engaged on actin. The cytoskeletal stress and strain generated in the cell are denoted as σ and ϵ, respectively. In the quiescent (non-adhered) state in the absence of mechanosensitive signaling, we assume myosin motors in the cell display some level of contractility, ρ_0, determined by a balance between the decrease in enthalpic interactions when motors bind to actin and the associated loss in entropy compared to free motors in the cytosol.

2.1.1 Conservative energy contributions to the metabolic potential: As a cell adhered to microposts evolves towards a dynamic steady state, part of the energy available from the hydrolysis of ATP is converted into other forms of energy associated with the assembly of new stress fibers, namely, i) the chemical energy required for myosin to bind to actin ($U_{binding}$), ii) the work done by the myosin motors (U_{motor}), and iii) the strain energy of the cytoskeleton (U_{strain}^{cell}) and the microposts (U_{strain}^{p}) (refer to SI Section 1 for more details) while the rest is dissipated as heat (Figure 2b). We denote the corresponding energy densities (energy per unit volume) with F; for example, $F_{binding}$ is the energy density associated with myosin motors engagement and in the case of cells on microposts, $U_{binding} = F_{binding}V_C$, where V_c is the cell volume. The myosin binding energy, $U_{binding}$, is the energy associated with the formation of actin-myosin bonds and represents the energetic cost of increasing the contractility from its quiescent state, ρ_0. The motor work, U_{motor}, represents the work done by the myosin motors in deforming the cytoskeleton and can also be thought of as the potential energy of the motors (see SI Section 1.1.2). The strain energy of the cell can be expressed in terms of the elastic modulus (K), (which represents the stiffness of the cytoskeleton including microtubules, actin and intermediate filaments), and the cytoskeletal strain, ϵ, while the strain energy of the microposts similarly can be expressed in terms of the stiffness of the microposts, K_p, and the strain due to cellular contraction, ϵ_p. We now define

the conservative part of the metabolic potential as $U_c(\rho,\epsilon) = U_{binding} + U_{motor} + U_{strain}^{cell} + U_{strain}^{p}$, which can be further expanded as:

$$U_c(\rho,\epsilon) = \left(\underbrace{\frac{\beta}{2}(\rho-\rho_0)^2}_{\substack{Myosin\ binding \\ energy\ density}} + \underbrace{\rho\epsilon}_{\substack{Motor\ work \\ density}} + \underbrace{\frac{K}{2}(\epsilon^2)}_{\substack{Cell\ strain \\ energy\ density}} \right) V_c + \underbrace{K_p \epsilon_p^2 l_p^2}_{\substack{Strain\ energy \\ of\ the\ two \\ posts}} \tag{1}$$

Here l_p is the distance between the microposts and β is a "chemical stiffness," which penalizes deviation of the contractility from its quiescent value determined by a competition between entropy of motors in the cytosol and the enthalpy of motors engaged to the cytoskeleton. The quadratic dependence of the myosin binding energy on the motor density is motivated by the fact that the quiescent state contractility represents an optimum and any deviation from it would lead to an increase in the energy of the system.

2.1.2 Kinetics of stress fiber assembly and steady state energy dissipation: We now derive the condition for the dynamic steady state of the cell constrained by the posts from a first-principles consideration of cytoskeletal kinetics and contraction based on the second law of thermodynamics. If the rate of engagement and disengagement per unit volume of myosin motors to the cytoskeleton is denoted $J_{on} > 0$ and $J_{off} > 0$, respectively, we can write the rate of change of ρ as $\frac{\partial \rho}{\partial t} = J_{on} - J_{off}$. For each motor that binds to actin filaments (stress fibers), ATP is hydrolyzed to release energy $(\Delta G/\rho_0)$ which we denote as $\Delta\tilde{G}$. Here, ΔG is the energy released per unit volume due to ATP hydrolysis in the quiescent cell. The energy available through ATP hydrolysis per unit time per cell due to motor activity throughout the entire cell is then $J_{on}\Delta\tilde{G}V_c$. Part of this energy is dissipated as heat, while the rest is converted into the conservative forms of energy (Figure 2b). The heat dissipated per unit time $\dot{D}$, can be found as the energy available through ATP hydrolysis minus the energy stored in conservative forms as a result of motor engagement and disengagement:

$$\begin{aligned} \dot{D} = & \underbrace{J_{on}\Delta\tilde{G}V_c}_{\substack{energy \\ from \\ ATP\ per\ unit\ time}} - \underbrace{J_{on}\left(\frac{\partial U_c}{\partial \rho}\right)}_{\substack{rate\ of\ conservative \\ energy\ change \\ upon\ motor\ engagement}} + \underbrace{J_{off}\left(\frac{\partial U_c}{\partial \rho}\right)}_{\substack{rate\ of\ conservative \\ energy\ change \\ upon\ motor\ disengagment}} \\ = & -J_{on}\left(\frac{\partial U_c}{\partial \rho} - \Delta\tilde{G}V_c\right) + J_{off}\left(\frac{\partial U_c}{\partial \rho}\right) \geq 0. \end{aligned} \tag{2}$$

We invoke the second law of thermodynamics which states that the dissipation rate should always be greater than zero, and hence choose the following forms for J_{on} and J_{off} :

$$J_{on} = -k_{on}(\sigma)\left(\frac{\partial U_c}{\partial \rho} - \Delta\tilde{G}V_c\right) \text{ and } J_{off} = k_{off}(\sigma)\left(\frac{\partial U_c}{\partial \rho}\right). \tag{3}$$

where k_{on} and k_{off} are positive rate parameters that govern myosin motor engagement and disengagement, respectively (Figure S1). A functional dependence of these parameters on the cytoskeletal stress σ is introduced to account for the mechano-sensitive upregulation in motor engagement and their subsequent stabilization under stress (Eq S1.19, refer to SI Section 1.2). At steady state, a dynamic equilibrium reflecting the elevated rates of mechano-signaling is established and the rate of motor engagement is balanced by the rate of disengagement, i.e., $J_{on} = J_{off}$, and the contractility remains constant over time. Enforcing this condition leads to

$$J_{on} - J_{off} = -\frac{\partial U_c}{\partial \rho}\Big(k_{on}(\sigma) + k_{off}(\sigma)\Big) + k_{on}(\sigma)\Delta\tilde{G}V_c = 0, \quad (4)$$

The above equation relates contractility to stress by accounting for the kinetics of stress fiber assembly and disassembly. As we show below, when $k_{on}(\sigma)$ increases and $k_{off}(\sigma)$ decreases with stress, more motors are recruited with increasing stress. It should be noted that the steady state heat dissipation rate obtained from Eq 2 is $J_{on}\Delta\tilde{G}V_c$, implying that all the energy released by myosin ATP consumption is dissipated as heat at steady state. The above analysis for myosin binding can also be further extended to the case of kinetics of contraction or motor movement along the actin filaments (refer to SI Section 1.1.4 for derivation). We find a Hill-like relation between rate of contraction and stress (Eq S1.17) that emerges as a natural consequence of the Second Law of Thermodynamics. Note that the energy dissipated due to motor friction during contraction can also be calculated, but since motors cease to move in the "stall" state (or steady state) when the cytoskeletal stress σ equals the stall stress, σ_m (Eq S1.18c), the velocity of contraction, $\dot{\epsilon}$, is zero), and there is no contribution to overall dissipation in this case. Next, we describe the energy available from ATP hydrolysis during myosin motor contraction considering the mechano-sensitive character of the rate parameters k_{on} and k_{off}.

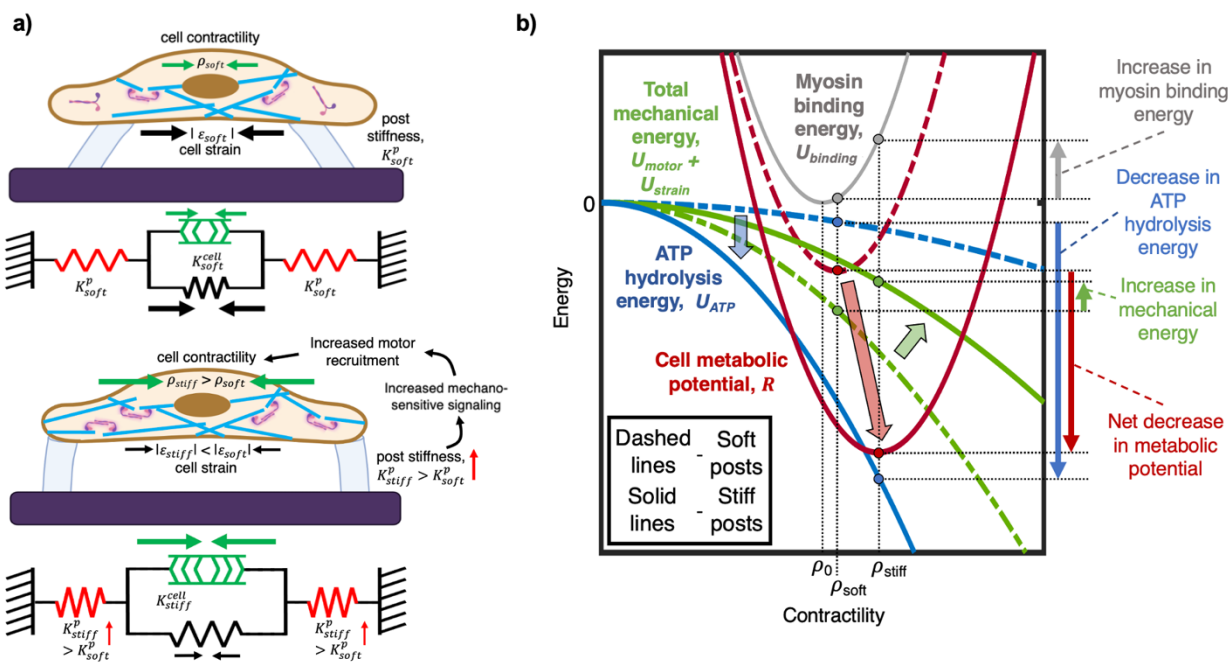

Figure 1: Metabolic potential for a cell on stiff and soft microposts. (a) Schematic depiction of a cell adhered to microposts described by a model with active contractile element representing myosin motors in parallel with a linear elastic spring that describes passive cytoskeletal components. For stiff microposts, mechanosensitive pathways upregulate motor activity leading to the development of more contractility with smaller strains. (b) Schematic of contributions to the metabolic potential for cells adhered to microposts as a function of contractility. On stiff microposts, higher stress leads to a higher net density of bound motors (ρ_{stiff}) than on soft microposts (ρ_{soft}) which leads to an increased myosin binding energy. Mechanical energy decreases in magnitude with stiffness of the posts because in a stiff environment the cell is not able to sustain large deformations or motor work. The larger energy from ATP hydrolysis in stiff environments drives these energetically unfavorable processes and leads to a net decrease in metabolic potential of the cell.

2.1.3 Energy associated with ATP hydrolysis: The hydrolysis of ATP is downhill energetically, and studies have estimated the value of energy released at ~50-70 kJ/mol[35]. Active non-muscle myosin-II motors utilize ATP hydrolysis to power a conformational change in the motor that facilitates the formation of crosslinks between actin and myosin and subsequent force

generation[30]. The amount of ATP hydrolyzed by myosin activity in a cell is dependent on the number density of engaged motors and the time over which they remain engaged. Therefore, the rates of motor binding $k_{on}(\sigma)$ and unbinding $k_{off}(\sigma)$ from actin must be considered to determine the amount of ATP motors hydrolyze. Physically, these rate parameters are related to the time over which the motors remain engaged/disengaged. Particularly, a low rate of motor disengagement implies that the motor remains engaged for a longer time i.e. $k_{off} \propto \left({}^{1}/_{\tau_{off}}\right)$, where τ_{off} is the time over which the motors remain engaged to actin (Figure S1). Both these rate parameters depend on the cytoskeletal stress, σ, for two reasons. First, tensile forces transmitted to the cytoskeleton activate stress-sensitive ion channels[33] and promote Ca^{2+} influx which upregulates the rate of motor binding (k_{on}) through phosphorylation of the myosin light chain kinase (MLCK)[36]. Second, stress-activated signaling molecules (such as Src family kinases) act on Rho-GTPases and enhance Rho activity which promotes ROCK mediated phosphorylation of myosin phosphatase (MYPT) (Figure 2a), leading to lowered myosin unbinding rates (k_{off})[31].

As the kinetics of mechano-sensitive myosin recruitment and release can depend on the cell type and the myosin II isoform in question, we consider here the properties of the two major non-muscle myosin isoforms in most cell types-myosin IIA and myosin IIB[37]. It has been reported that the rate of motor disengagement (k_{off}) decreases under tension for myosin IIB, due to its strong catch-bond properties[38]. However, an increase in myosin IIB recruitment (k_{on}) in response to force is much less prominent and cell type specific[39], and depends on IIB copolymerization with IIA[40]. On the other hand, myosin IIA is strongly recruited by actin filaments (the on-rate k_{on} increases) under tension[38], but its catch bond behavior is much weaker than that of IIB[40]. Hence, if we assume the on-rate to be an increasing function of stress and the off-rate to be a decreasing function of stress, the enhanced sensitivity of myosin IIA recruitment to stress and the strong catch-bond property of myosin IIB are captured (Eq S1.19). Thus, this functional dependence on stress assigned to the two rates accounts for both the effects of mechano-signaling affecting motor activation and the properties of different myosin isoforms on the kinetics of the myosin work cycle. The overall effect is that, on stiff substrates, the dynamic equilibrium of the population of myosin motors in a cell considering both isoforms shifts towards the engaged state (Figure S1), leading to a larger amount of energy available through ATP hydrolysis (Figure 2b). The fraction of the time over which a myosin motor is engaged to actin stress fibers and hydrolyzes ATP can be written in terms of the rates as $\tilde{\tau} = \frac{k_{on}(\sigma)}{k_{on}(\sigma)+k_{off}(\sigma)}$; when the binding rate is high and the unbinding rate is small, normalized myosin motor engagement time becomes close to unity. Then the *time-averaged* energy released by ATP hydrolysis due to myosin activity when the cell reaches a steady state can be written (SI Section 1.1.4) as:

$$U_{ATP} = -\underbrace{\tilde{\tau}}_{\substack{\text{Fraction of time}\\ \text{for which motors}\\ \text{remain engaged}}} \times \underbrace{\left(\frac{\Delta G}{\rho_0}\right)}_{\substack{\text{Energy released}\\ \text{due to a single}\\ \text{motor binding}}} \times \underbrace{\rho}_{\substack{\text{Number density}\\ \text{of engaged}\\ \text{motors}}} \times V_c \tag{5}$$

Here $\tilde{\tau}\rho$ represents the time-averaged density of engaged motors that hydrolyze ATP and do mechanical work, while $\Delta G/\rho_0$ is a measure of the amount of energy released by a single myosin motor.

2.1.4 A metabolic potential for adherent cells: Next, we introduce the metabolic potential, R, as the sum of all energetic contributions, both conservative and the energy from ATP hydrolysis: $R = U_c + U_{ATP}$. Since it accounts for all energetic contributions and the effective kinetics of myosin recruitment, we can minimize the metabolic potential with respect to contractility and strain to

predict the steady-state optimum configuration for the cell. Minimization with respect to contractility gives the following expression:

$$\frac{\partial R}{\partial \rho} = \underbrace{\frac{\partial U_c}{\partial \rho}}_{\substack{Conservative\ energy \\ change\ on \\ motor\ binding}} + \underbrace{\frac{\partial U_{ATP}}{\partial \rho}}_{\substack{Change\ in \\ ATP\ energy\ on \\ motor\ binding}} = \frac{\partial U_c}{\partial \rho} - \left(\frac{\Delta G}{\rho_0}\right)\frac{k_{on}(\sigma)}{k_{on}(\sigma) + k_{off}(\sigma)} V_c = 0. \tag{6}$$

which provides a relation between the contractility and the stress, governed by the *kinetics* of mechanochemical signaling. Similarly, minimizing the metabolic potential with respect to strain, we obtain a relation for the strain (contraction) of the cell:

$$\frac{\partial R}{\partial \epsilon} = (K\epsilon - \sigma + \rho) = 0. \tag{7}$$

Equation 7 is the condition for balance of forces; the stress generated by the cell is equal to the sum of active (contractility, ρ) and passive stresses ($K\epsilon$) (refer to SI Section 1.2 for derivation of steady state contractility and strain). Further, Equation 6 is the same as Equation 4 that predicted the dynamic steady state based on the kinetics of myosin motor contraction. *Hence, minimizing the metabolic potential of the cell with respect to contractility and strain is equivalent to predicting dynamic steady state on the basis of myosin motor engagement and disengagement consistent with the Second Law of Thermodynamics.*

2.2 Predictions of steady state energy for cells adhered to microposts

We now examine how the energies describing the cell-micropost system (Eqs 1 and 5) change with respect to contractility, ρ, and stiffness of the posts, K_p. The myosin binding energy, $U_{binding}$, and the energy of ATP hydrolysis, U_{ATP}, are plotted as a function of contractility in Figure 1b for two different values of post stiffness representing a soft (~1.5 nN/μm) and a stiff (~30 nN/μm) system, which fall within the stiffness range reported for microposts fabricated to examine the effect of rigidity on mesenchymal cells[41]. Also depicted is the mechanical energy, which is the sum of motor work, U_{motor}, and the strain energy of deformation associated with the cell, U_{strain}^{cell}, and microposts, U_{strain}^{p} (Figure 1b). We observe the following trends:

- *Myosin Binding Energy*: The binding energy represents the energetic cost of increasing or decreasing the number density of engaged motors from its quiescent value, ρ_0. In the case of cells adhered to stiff microposts, the upregulation of myosin motor recruitment due to stress-activated signaling pathways (see Figure 2a) leads to a large increase in the contractility from its quiescent state value, ρ_0, and is associated with higher myosin binding energy (Figure 1b). By contrast, in cells adhered to soft microposts, the cytoskeletal stress developed is low and the increase in contractility from the quiescent state is not as large, leading to lower binding energy values (Figure 1b).
- *Mechanical Energy*: This represents the sum of the motor work and the elastic strain energy of the cell. The former is a measure of the potential energy of myosin motors, and by extension, the work done by motors in deforming the cytoskeleton and microposts. As cell contraction increases, the work done by the motors increases and is associated with a decrease in their potential energy. This mechanical work is stored as strain energy of the passive components including the cytoskeleton and microposts which increases with cell contractility. Note that when the cell deforms, the motor potential energy always decreases by twice the amount that the strain energy increases. (Eqs S1.23-S1.24). This arises from the fact that motors act as force dipoles, so any amount of strain energy they impart translates to their potential energy decreasing by double the amount. Thus, greater levels of contractility of the cell leads to lower potential energy and hence also lower

overall mechanical energy for a given post stiffness (Figure 1b). On stiffer posts, the mechanical energy increases for all levels of contractility (ρ), leading to an upward shift in the curve (Figure 1b). Note the monotonicity of these trends depends on the relative stiffness between the cell and post, as further described in SI Section 1.2 and Figure S3.

- *Energy of ATP hydrolysis*: While the mechanical energy and myosin binding energy is higher for cells adhered to stiffer microposts, more energy is available from ATP hydrolysis in this case due to increased motor activity. On soft microposts, stresses

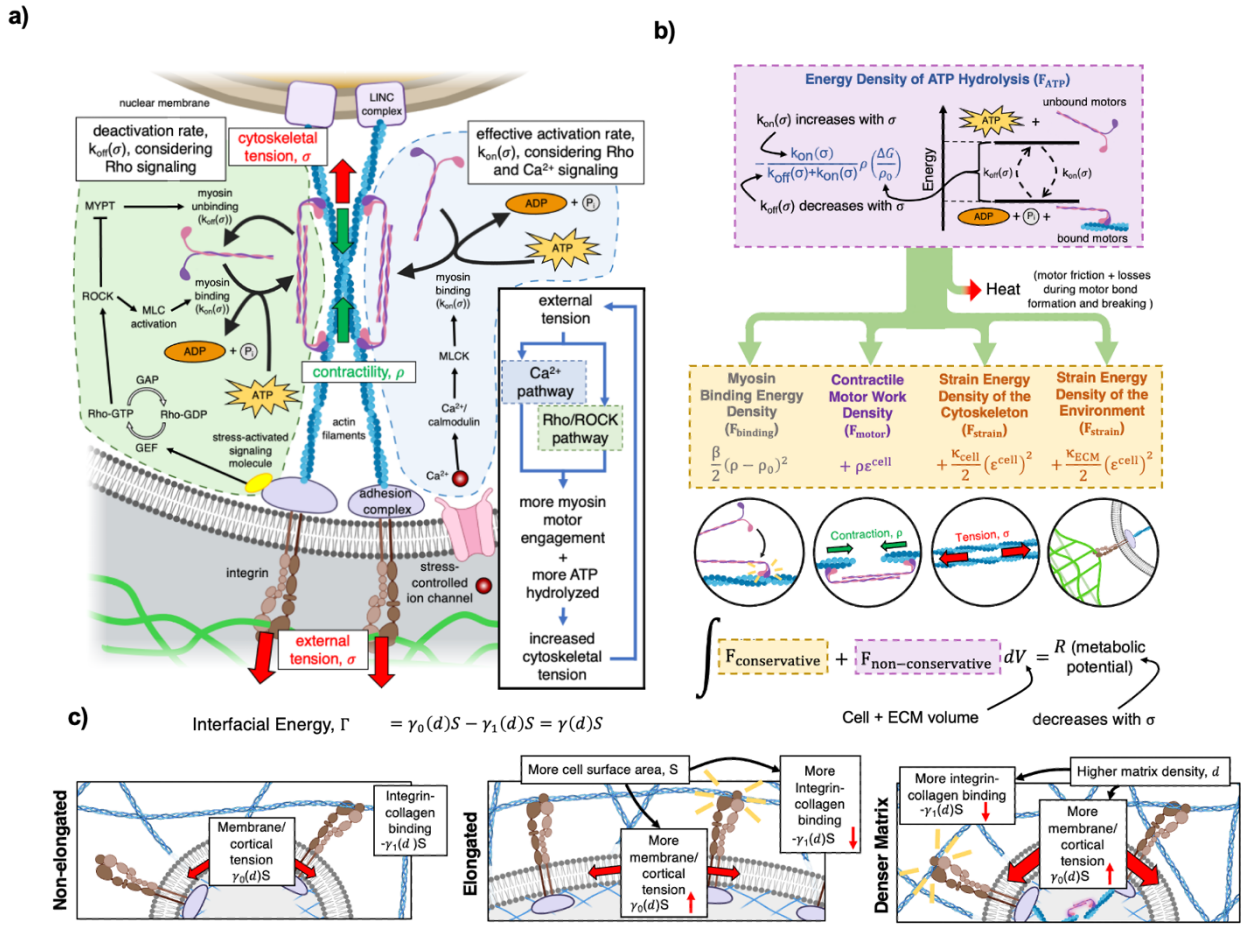

Figure 2: A model for the establishment of stress-regulated contractility driven by ATP hydrolysis. (a) Schematic illustrating the stress-dependent pathways (Rho-ROCK and Ca^{2+} pathways) that regulate cell contractility. Tensile forces transmitted from the micro-environment act on adhesion complexes at the cell membrane and trigger the following bio-chemical processes: (I) The stress-assisted activation of signaling molecules (like Src Family Kinases (SFKs)), which act on Rho-GTPases and enhance Rho activity, promoting ROCK-mediated phosphorylation of myosin light chain (MLC) and consequently, motor recruitment. ROCK activation also leads to inhibition of myosin phosphatase (MYPT) which downregulates myosin unbinding. (II) The generation of cell membrane tension leading to the opening of stress-controlled ion-channels resulting in an influx of Ca^{2+} into the cytoplasm and upregulation of motor activation by myosin light chain kinase (MLCK) activation. Both processes lead to a net increase in the density of bound motors and more ATP hydrolysis. (b) Schematic showing the breakdown of energies considered in the metabolic potential for the cell. The energy released by ATP hydrolysis (F_{ATP}) depends on the kinetics of motor binding/unbinding and comprises the dissipative part of the energy, some of which is converted into conservative forms such as the work done by myosin motors in deforming the cytoskeleton (F_{motor}), the chemical energy required to bind myosin motors to actin filaments ($F_{binding}$), and the strain energy of deformation of the cytoskeleton and ECM (F_{strain}), while the rest is dissipated as heat. (c) The interfacial energy in our model is comprised of two contributions: the membrane/cortical tension, γ_0, which resists any increase in the cell surface area and the adhesion energy of integrin-collagen binding, γ_1, which favors cell elongation as more integrin-ligand bonds can form on the increased surface area of an elongated cell.

experienced by the cell are small and the stress-enhanced increase in the contractility is not very large since there is only a modest increase in the on-rate and decrease in the off-rates of the motors. By contrast, on stiff microposts, due to the high magnitude of cytoskeletal stress developed by the cell as it contracts, the upregulation of motor recruitment through mechanosensitive signaling pathways is enhanced, leading to a much larger density of engaged motors and larger contractility at steady state (see Figure 2a). The magnitude of energy available through ATP hydrolysis is correspondingly larger on stiff microposts, as a larger amount of ATP is consumed to maintain the steady state contractility (Figure 1b).

Despite the unfavorable increases in binding energy and mechanical energy associated with establishing higher contractility, when coupled with ATP hydrolysis, which is an exothermic process, increases in contractility are favorable on stiffer posts. As discussed in Section 2.1.3, the stress-dependent kinetics of motor engagement and disengagement determines the time-averaged amount of energy available from ATP hydrolysis. Stiffer environments favor the recruitment of motors because these rates depend on cytoskeletal stress ($k_{on}(\sigma)$ increases with σ and $k_{off}(\sigma)$ decreases with σ), establishing positive feedback between stress-activated signaling and contractility in our model. We solve Equations 3 and 4 to determine the steady state contractility, strain and stress as a function of micropost stiffness (Eqs S1.26a-c) as well as how the individual energies change with contractility and post stiffness (Eqs S1.23-S1.25). These trends are plotted in Figure 1b, as is the trend in metabolic potential. We find the minimum in the metabolic potential predicts an increasing level of steady state contractility with micropost stiffness driven by the larger rate of decrease in ATP hydrolysis energy with contractility on stiffer posts. While both the contractility on soft posts (ρ_{soft}) and the contractility achieved on stiff posts (ρ_{stiff}) are larger than the quiescent value (ρ_0), the level of steady state contractility is higher for cells on stiff posts ($\rho_{stiff} > \rho_{soft}$) due to more stress-dependent mechanosensitive upregulation of myosin motor recruitment. An alternative schematic that summarizes these changing trends in predicted energy values with microenvironment stiffness is provided in Figure S4.

2.2.1 Determination of the biophysical parameters in the metabolic potential model: To validate our model, we consider experiments performed by Mitrossilis et al. in which myoblasts were allowed to contract between two parallel fibronectin-coated glass plates[42]. One plate was rigid, while the other was flexible and acted as a nano newton force sensor. The traction force exerted by the cell on the flexible plate as it spreads was measured and found to be directly proportional to the cell contractility. On treatment with blebbistatin which inhibits myosin activity, the force generated by the cells decreased, establishing the direct correlation between force and myosin mediated contractility. To assess the effect of the stiffness of the micro-environment on force generation, flexible plates of different stiffnesses were used and the force generated by the cell was measured as a function of the stiffness. To accurately predict the force with our model, we need to determine the chemical stiffness β, the quiescent state contractility ρ_0 and the rate parameters governing motor engagement and disengagement, $k_{on}(\sigma)$ and $k_{off}(\sigma)$, respectively. In a previous study, the static contractility for cardiac tissues[43] contracting against deformable micro-cantilevers was estimated to be $0.5\ kPa$. Similar values were reported for the contraction of fibroblasts confined in a 3D collagen matrix[44]. Hence, we assume the isotropic contractility ρ_0 to be $0.5\ kPa$.

As described earlier, stress-activated signaling pathways enhance the rate of myosin motor recruitment (Figure 2a). Hence, we assume $k_{on}(\sigma)$ to be a linear, monotonically increasing function of the cytoskeletal stress, $k_{on}(\sigma) = k_{on}^0 \alpha \sigma$, where α is a chemo-mechanical parameter representing the effect of signaling pathways and k_{on}^0 is the binding rate constant for myosin in the quiescent state. Similarly, motors are stabilized due to external stress and hence we assume

$k_{off}(\sigma)$ to be a linear, monotonically decreasing function of stress, $k_{off}(\sigma) = k_{off}^0(1 - \alpha\sigma)$, where k_{off}^0 is the unbinding rate constant for myosin in the quiescent state. Assuming that the myosin motor association and dissociation constants are nearly identical in the quiescent state $(k_{on}^0 \sim k_{off}^0)$, the energy available through ATP hydrolysis now reduces to the form $U_{ATP} = -\alpha\sigma\rho V_c$, which maintains that stress enhances the energy available through ATP hydrolysis. Based on these assumptions, we derived an expression for the force exerted by the cell (Eq S1.32, refer to SI Section 1.2.1), and identify that it depends on two parameters, namely, an effective stiffness $\bar{k}$ and $\bar{F}$ which is the stall force exerted by the cell on the plates. The stall force $\bar{F}$ and the effective stiffness $\bar{k}$ (Eq S1.33) were estimated by curve fitting with a least squares method the force predicted by the model[34] against experimental measurements of force exerted by myoblasts on the deformable plate[42]. With these two quantities, we can now determine the chemical stiffness β and the chemo-mechanical coupling parameter α from Eq S1.34. These values are listed in Table S1 and are used in our subsequent simulations of mesenchymal cell behavior in 2D and 3D micro-environments.

2.3 A 3D chemo-mechanical formulation of the metabolic potential

Here, we briefly describe (refer to SI Section 2 for details) a general 3D model for a contractile cell that follows the basic ideas outlined in the example of a cell adhered to microposts. The key mechanical components of this model are: a) stress fibers comprised of active contractile elements in parallel with passive components representing the cell cytoskeleton, b) a poroelastic nucleus, c) adhesions that provide a mechanical connection between the cell and microenvironment and d) the extracellular matrix or substrate.

A) The stress fibers: In the 3D model, we treat the contractility, stress, and strain fields as tensor variables because the cell can adopt non-spherical shapes that generate spatially non-uniform anisotropic stresses and motors can be polarized or oriented in different directions at a given location in the cell (Figure 3a). In this case, the contractility fields (motor densities associated with stress fibers) are anisotropic i.e., $\rho_{11} \neq \rho_{22} \neq \rho_{33}$ as are the stresses. Also, the stresses and contractility can vary spatially across the cell body, hence we consider these quantities to depend on the spatial co-ordinates, $\mathbf{x}$. The volumetric part of the contractility tensor $\rho_{kk}(\mathbf{x}) = (\rho_{11}(\mathbf{x}) + \rho_{22}(\mathbf{x}) + \rho_{33}(\mathbf{x}))/3$ represents the cell contraction averaged over all directions and hence is a measure of the number of engaged motors per unit volume (Figure 3a), where $\mathbf{x}$ denotes the spatial coordinates in the cell. The deviatoric part of the contractility, $\tilde{\rho}_{ij}(\mathbf{x}) = \rho_{ij}(\mathbf{x}) - (1/3)\rho_{kk}(\mathbf{x})\delta_{ij}$ is a measure of the deviation of each component of contractility from the mean and can be considered to represent the extent of polarization of motors or actin stress fibers. Like the micropost model, we define the conservative energy densities, namely the myosin binding energy (Eq S2.8), motor work (Eq S2.9) and the strain energy of the passive components (Eq S2.10)) at every point in the cell. The energy of ATP hydrolysis is defined in a similar manner as Eq 2 (see Eq S2.12a), but now the rate parameters governing stress fiber assembly k_{on} and disassembly k_{off} are anisotropic tensor quantities themselves (refer SI Section 2.2 for tensorial description of energies). The on- and off-rates can further be decomposed into a volumetric and deviatoric part (Eqs S2.12b, c): the volumetric parts of which ($k_{on}^v(\sigma_{kk}(\mathbf{x}))$ and $k_{off}^v(\sigma_{kk}(\mathbf{x}))$) capture overall change in binding rates dependent on mean stress (i.e., $k_{on}^v(\sigma_{kk}(\mathbf{x})) = (k_{on,11}(\sigma_{kk}(\mathbf{x})) + k_{on,22}(\sigma_{kk}(\mathbf{x})) + k_{on,33}(\sigma_{kk}(\mathbf{x}))/3)$, and the deviatoric parts of which ($\tilde{k}_{on,ij}(\tilde{\sigma}_{ij}(\mathbf{x}))$ and $\tilde{k}_{off,ij}(\tilde{\sigma}_{ij}(\mathbf{x}))$) capture anisotropy in myosin engagement rates due to stress polarization. We adopt this tensorial implementation for the myosin motor engagement and disengagement rates because although individual motor binding events are upregulated by the activation of stress-regulated signaling pathways[38,40] (Figure 2a), the overall alignment and

assembly of stress fibers is also found to be influenced by the cytoskeletal stress. For example, stress fiber formation was found to increase with the rigidity of the microenvironment in both mesenchymal and endothelial cells[45], and overall alignment is highly dependent on cell shape[46]. The specific functional dependence of the on and off rates on stress that we use is given in Eq S2.31 and the resulting form for the energy available through ATP hydrolysis is given in Eq S2.30.

B) Adhesions at the cell-matrix interface: Transmembrane proteins at the cell-ECM interface, such as integrins, form a bond with ligands on the ECM and play an important role in transmitting forces to the cell cytoskeleton. To capture the cellular morphology in 2D and 3D micro-environments, we also introduce an interfacial energy, Γ, which is a function of the cell shape. There are two contributions to the interfacial energy: the cell surface tension, γ_0, that resists any increase in the cell area or elongation and an adhesive contribution from membrane protein-ligand interactions, γ_1, that favors an increase in cell surface area along the cell-matrix interface (Figure 2(c)). Cell membranes consist of lipid bilayers tethered to an underlying rigid actin-myosin cortex. Hence, any change in the cell membrane area is accompanied by unfavorable stretching of membrane-engaged proteins that resist an expansion in cell area as well as by the sustained contraction of the underlying actomyosin cortex. We consider these effects to represent the energetic cost of stretching the cell membrane. The adhesive element represents the reduction in energy achieved due to bond formation between receptors such as integrin at the cell-matrix interface and ligands present in the matrix. The relative strengths of these two quantities determine whether total interfacial energy $\Gamma = \left((\gamma_0 - \gamma_1)S\right)$ will increase or decrease with cell surface area, S (Figure 2c). An equation to estimate the adhesive energy is presented in SI Section 2.2.6 (Eq S2.39)), and a rough estimate of the receptor-ligand energy is found to be of the order of $\sim 10^{-6} N/m$. Typical membrane tension values[47] for the cell are of the order of $\sim 10^{-4} - 10^{-5} N/m$, therefore, we consider the effective interfacial energy a positive quantity that increases with cell surface area. Additionally, as the density of the ECM, d, increases, the number of ligands available increases and the adhesive energy becomes increasingly negative, i.e., γ_1 is a function of d and increases with collagen density. However, it has been observed that the membrane tension also increases with matrix stiffness ($\gamma_0 = \gamma_0(d)$). Up to a threefold increase in the membrane tension has been observed for hepatic myofibroblasts[48] as the ECM stiffness is increased from 4 to 25 kPa. Hence, the total interfacial energy can be an increasing or decreasing function of collagen density depending on the relative strength of γ_1 and γ_0. As the membrane tension is two orders of magnitude larger than the energy of receptor-ligand adhesions, we choose the interfacial energy, $\Gamma = \left((\gamma_0(d) - \gamma_1(d))S\right) = \gamma(d)S,$ to be an increasing function of collagen density (Figure 2c), where $\gamma(d)$ is the difference between γ_0 and γ_1. The ligands transmit tensile forces from the ECM to the cytoskeleton, and in a coarse-grained approach we treat the receptor-ligand bond as an elastic layer with mechanical properties $E_{integrin}$ and $\nu_{integrin}$, representing their effective Young's modulus and Poisson's ratio, respectively (Table S4).

C) The nucleus: As water influx/efflux and fluid redistribution are the chief modes of nuclear deformation in response to stress, the nucleus can be considered a poroelastic solid. However, the timescale of poroelastic and viscous relaxation in the nucleus has been measured to be ~80s[49], which is very rapid compared to the time it takes for cell spreading[50]. We therefore model the nucleus as a linear elastic spheroidal inclusion encapsulated within the cell with elastic properties K_{nuc} and μ_{nuc} denoting its bulk and shear modulus, respectively, while the strain experienced by the nucleus is denoted by ϵ_{ij}^{nuc}. These properties represent the mechanical moduli of the nucleus after it has relaxed from viscous effects. Transmission of force from the cytoskeleton to the nuclear envelope is facilitated by LINC complex proteins[51], and to account for

effective force transmission to the nucleus, we model the nesprins as a softer thin, elastic layer around the nucleus.

D) Mechanical response of the microenvironment: We consider two types of cell micro-environments in this work: 1) cells encapsulated in 3D collagen, and 2) cells seeded on 2D PA gels. The mechanical behavior of collagen is modelled using a fibrous non-linear constitutive model. While the elastic modulus of PA gels can be tuned by varying the monomer (acrylamide) and cross-linker (bis-acrylamide) concentrations, AFM measurements showed that gels with

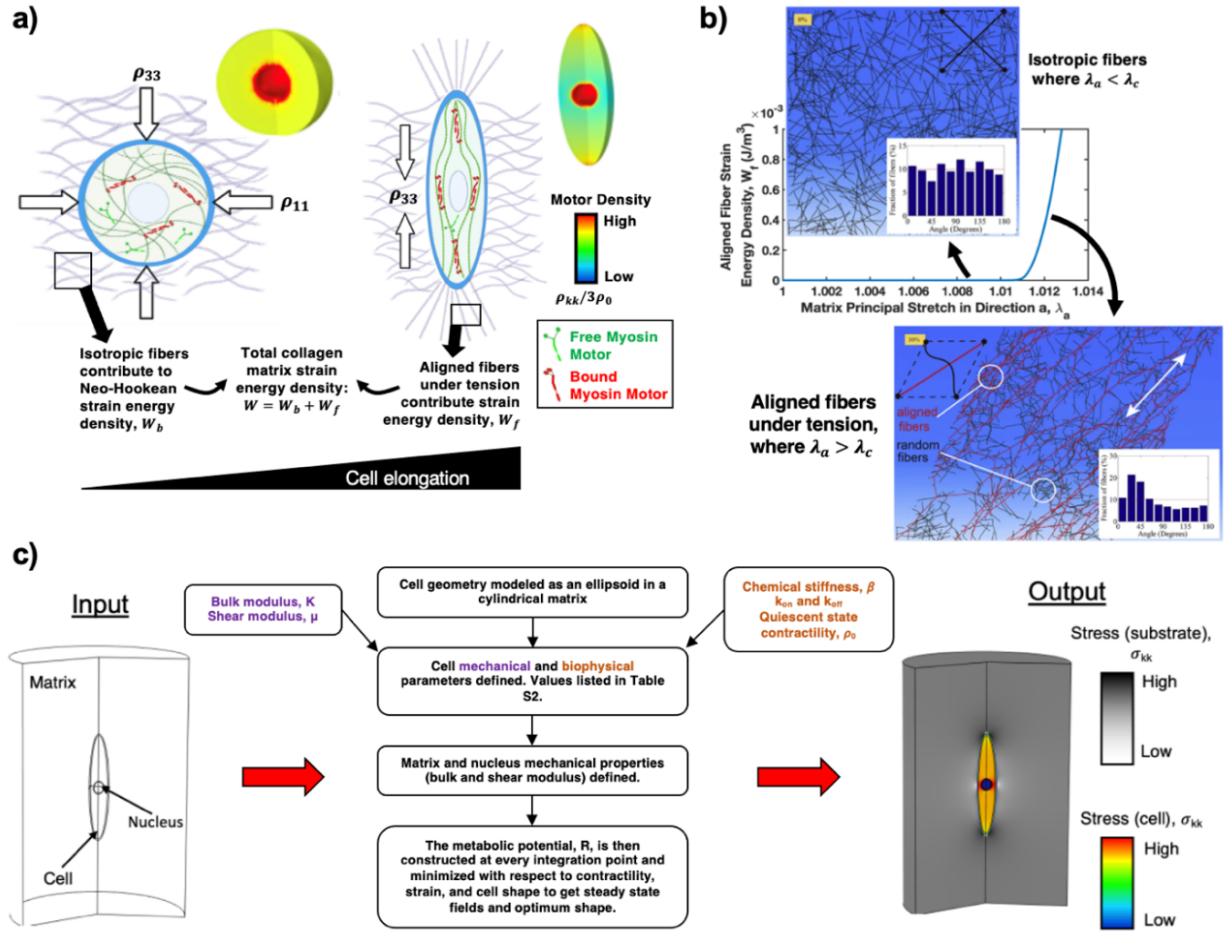

Figure 3: Determination of the cell shape, contractility and stress fields using the metabolic potential within a finite element framework, illustrated for cells in 3D collagen gels. (a) Depiction of the tensorial nature of contractility and a schematic illustrating the non-linear fiber model used to represent collagen which captures the preferential alignment of fibers along the direction of maximum principal stretch λ_a, (b) Graphical illustration of the strain energy density function $f(\lambda_a)$ along with representation of fiber alignment beyond a critical stretch λ_c as reported from discrete fiber simulations[53], and (c) Flowchart depicting the method of solution employed along with workflow for determining the steady state strain and contractility fields.

stiffness values of physio-pathological relevance exhibited ideal linear elastic behavior even at the nanometer scale[52]. The 2D PA gel is therefore modelled as a linear elastic material. Following our previous work[53], the mechanical behavior of the collagen network is determined by considering fibers that preferentially align along the direction of maximum principal stretch, whose strain energy density is given by W_f, and another orthogonal set of fibers that do not align and display an isotropic mechanical response, which has a strain energy density W_b (Figure 3a, Eq S2.35). The strain energy of the aligned fibers, W_f, is given by the energy function $f(\lambda_a)$ (see Eq

S2.36) which is chosen, such that (i) W_f vanishes below a critical value of tensile stretch, λ_c (Figure 3b), and (ii) the matrix stiffens only in the direction of (tensile) principal stretches when the principal stretch, λ_a, is larger than the (tensile) stretch critical value (Figure 3b). The bulk and shear moduli of collagen as a function of its density were determined from experimental data where the equilibrium modulus of collagen was measured[17], as described in SI Section S2.2.5

2.4 Generalized 3D expression for the metabolic potential of an adherent cell

Following the approach for the cell-micropost system, we first define the local metabolic potential R_p at every spatial co-ordinate $\boldsymbol{x}$ in a 3D context, by summing all energetic contributions, namely, (a) the conservative energy density which is comprised of the myosin binding, motor work and the strain energy densities of passive components and (b) the energy from ATP hydrolysis per unit volume which can be decomposed into volumetric and deviatoric parts as:

$$\begin{aligned} R_p\left(\rho_{ij}(\boldsymbol{x}), \epsilon_{ij}(\boldsymbol{x}), \Theta\right) &= \underbrace{F_c\left(\rho_{ij}(\boldsymbol{x}), \epsilon_{ij}(\boldsymbol{x}), \Theta\right)}_{Conservative\ contributions} \underbrace{-\frac{1}{3}\frac{k_{on}^{v}\left(\sigma_{kk}^{cell}(\boldsymbol{x})\right)}{k_{off}^{v}\left(\sigma_{kk}^{cell}(\boldsymbol{x})\right)+k_{on}^{v}\left(\sigma_{kk}^{cell}(\boldsymbol{x})\right)}\frac{\Delta G}{\rho_0}\rho_{kk}(\boldsymbol{x})}_{ATP\ hydrolysis\ energy\ due\ to\ motor\ recruitment} \\ &\underbrace{-\sum_{i=1}^{3}\sum_{j=1}^{3}\frac{\tilde{k}_{on,ij}\left(\tilde{\sigma}_{ij}(\boldsymbol{x})\right)}{\tilde{k}_{off,ij}\left(\tilde{\sigma}_{ij}(\boldsymbol{x})\right)+\tilde{k}_{on,ij}\left(\tilde{\sigma}_{ij}(\boldsymbol{x})\right)}\frac{\Delta G}{\rho_0}\tilde{\rho}_{ij}(\boldsymbol{x})}_{ATP\ hydrolysis\ energy\ due\ to\ cell\ polarization} \end{aligned} \quad (8)$$

where Θ is a variable containing information about cell shape, for example, the aspect ratio of an elongated cell. We note that R_p is a functional quantity due to the spatial dependence of $\rho_{ij}(\boldsymbol{x})$ and $\epsilon_{ij}(\boldsymbol{x})$ and as such requires a functional derivative in order to minimize with respect to these quantities. Next, we can define the metabolic potential by integrating the local metabolic potential over the cell volume and adding the interfacial energy:

$$R = \int_{V_c} R_p\left(\rho_{ij}(x), \epsilon_{ij}(x), \Theta\right) dV_c + \Gamma(\Theta) \quad (9)$$

The cell metabolic potential represents the potential of a cell to enhance its contractility and alter its morphology/shape in response to the mechanical properties of its micro-environment by considering mechanosensitive cytoskeletal kinetics. Further, we define the volumetric part of the metabolic potential as the sum of the conservative and ATP energy densities integrated over the cell volume, i.e. $\upsilon^{cell} = \int_{V_c}(F_c + F_{ATP})\, dV_c$. As in the micropost example, the minimization of the metabolic potential with respect to the contractility, strain, and shape yields the rate of ATP consumption in the cell at steady state (Eq S2.28).

To determine the optimum cell shape and contractility as a function of matrix stiffness, we employ a finite element procedure as described in SI Section 2.3 (Figure 3c). Briefly, we construct cell geometries with varying cell body aspect ratio and discretize the geometry within a finite element framework. At every spatial co-ordinate $\boldsymbol{x}$, we determine the steady state cellular contractility and strain by minimizing the local metabolic potential R_p with respect to $\rho_{ij}(\boldsymbol{x})$ and $\epsilon_{ij}(\boldsymbol{x})$ by taking functional derivatives of R_p with respect to these variables. This yields a set of partial differential equations that we solve for a given cell body aspect ratio (Eqs S2.17a-b). Then, knowing the spatial variation of the contractility and strain, we determine the cell metabolic potential

R corresponding to a particular cell body aspect ratio by summing the local metabolic potential R_p integrated over the cell volume with the interfacial energy corresponding to that shape (Eq 9). This process is repeated for different cell body aspect ratios and the optimum cell shape is identified as the cell body aspect ratio that has minimum metabolic potential. We repeated this procedure for different matrix stiffness values to generate the variation of optimum cell shape and contractility with stiffness.

3 Results

3.1. Minimization of the metabolic potential predicts how the shape and anisotropic contractility of metastatic cancer cells depend on collagen density

The morphology, cytoskeletal contractility and bio-energetic requirements of cells encapsulated in a three-dimensional collagen matrix are tightly regulated by the density of the collagen network[17,54]. To understand what physical mechanisms govern the establishment of cellular morphology, cytoskeletal contractility, and metabolism, we use the 3D model for the metabolic potential to study the shapes and distribution of contractility in MDA MB-231 breast cancer cells in collagen. The cell body is modeled as an ellipsoidal inclusion with two semi-axes of equal radii and a third distinct radius ($a = c \neq b$), with the aspect ratio defined as $AR = {}^{a}/_{b}$ (Figure 4b). A $AR = 1$ corresponds to a spherical cell while $AR > 1$ represents elongated cells. We normalize the aspect ratio by the circularity, $circ = 4\pi\frac{cross-sectional\ area}{(perimeter)^2}$, which gives a quantity termed the elongation factor (EF) (see Figure 4b) to quantify the shape of cells. We further assume a constant cell volume of 5000 μm^3. This is a reasonable assumption, as cell volume is regulated through water transport in an out of the cell which requires extremely high osmotic pressures (~1 MPa)[55], around three orders of magnitude higher than the cytoskeletal tension observed in the cell (~1-10 kPa). The collagen matrix is modelled as a cylinder that ensconces the cell, with radius greater than 50 times that of the cell to reduce boundary effects. The mechanical behavior of collagen networks is described by a non-linear fiber model (see Section 2.2.5) that can represent the strain stiffening of collagen due to tension-induced realignment of collagen fibers (Figure 3b). We determine the steady state cell shape, strain and contractility by minimizing the metabolic potential, R (Eq 9) with respect to these variables within a finite element framework (Figure 3c). This process is repeated for collagen matrices of varying densities. An iterative analysis was performed where model predictions of cell elongation and contractility at steady state was compared against corresponding experimental measurements for MDA MB-231 cells to determine the mechanical and biophysical parameters and are listed in Table S4.

3.1.1 Cytoskeletal stress and rates of ATP hydrolysis are higher in elongated cells: First, our model predicts that the volumetric part of the metabolic potential, υ^{cell}, which includes the mechanical, myosin binding and ATP hydrolysis energies, is lower for elongated cells, as the levels of stresses are overall higher (Figure S5). At any given density of collagen, as the cell elongation is increased, the volume-averaged mean cytoskeletal stress ($\frac{1}{V_c}\int_0^{V_c}\frac{\sigma_{kk}}{3}dV_c$) increases, saturates then begins to decrease at very high elongations ($EF > 50$) (see Figure S5). The initial increase occurs because isotropic contraction of an elongated cell leads to the development of an anisotropic stress field with stress concentration near the elongated ends (Figure 4a). The localized stresses at the elongated ends activate mechano-transductive signaling pathways (Figure 2a) that upregulate motor recruitment and consequently ATP consumption along the elongated axis. By examining the deviatoric components of the stress, which represent polarization of stress fibers, we find that the deviatoric stress along the elongated axis, $\tilde{\sigma}_{33}$, is indeed higher than that along the other axes (see Figure S6). In this way, the anisotropic stress field due to elongated cell morphologies leads to preferential alignment of stress fibers.

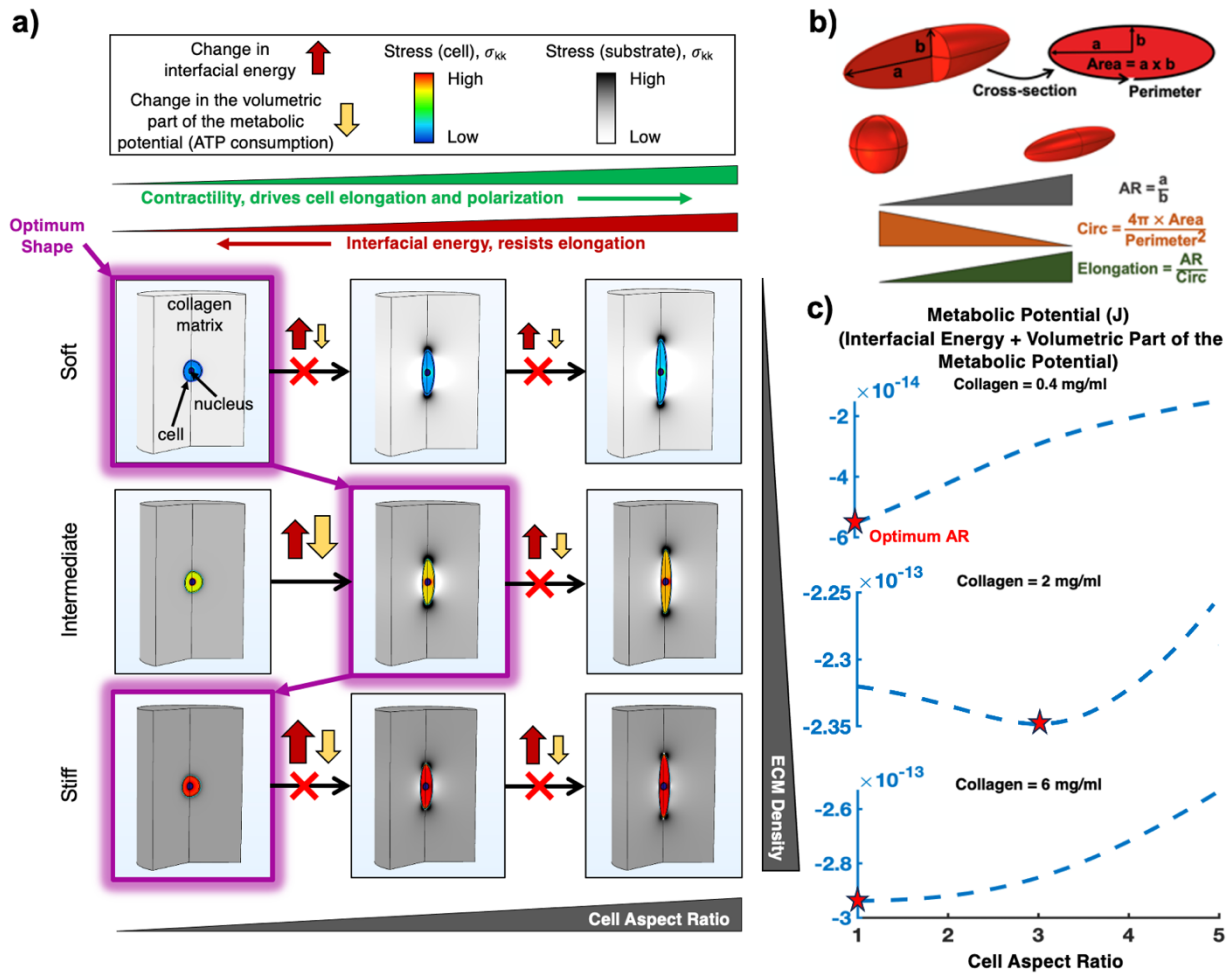

Figure 4: Minimizing the metabolic potential predicts a biphasic variation in cell shape with increasing collagen density. (a) Optimum cell shape shows a biphasic transition from spherical in low density collagen to elongated (spindle-shaped) in medium density collagen, back to spherical in high density collagen as a result of the competition between the volumetric part of the metabolic potential (red block arrows) and the interfacial energy (yellow block arrows). (b) Schematic description of cell body aspect ratio (AR), circularity (circ) and their variation with cell shape.(c) Metabolic potential as a function of cell shape for low (0.4 mg/mL), medium (2mg/mL) and high density (6 mg/mL) collagen, where the minimum in metabolic potential corresponds to the steady state optimum cell shape at all collagen densities.

Accordingly, for a given collagen density, the mean contractility $\frac{\rho_{kk}}{3}$ increases near the elongated ends (Figure 3a). As the stress generated by the initial isotropic cell contraction is larger on denser matrices, the extent of stress-regulated signaling is greater, leading to a higher density of engaged motors and consequently, for a cell of fixed elongation, higher contractility in dense collagen matrices (Figure S7). We find that the cell contractility, energy of ATP hydrolysis and the variation of the volumetric part of the metabolic potential with cell elongation closely resemble the underlying trend in volumetric stress (Figure S8a). With increasing elongation, the volumetric stress saturates because the increase in the stress along the direction of elongation, σ_{33}, is now balanced by the decrease in stress along the other two directions, σ_{22} and σ_{11} (Figure S5). This is a consequence of the fact that the cell volume is nearly constant, which requires that elongation along one direction be accompanied by equal levels of contraction along the other two directions.

3.1.2 Optimum cell aspect ratio determined by minimizing the metabolic potential shows a biphasic variation with collagen density. Next, we consider the effect of interfacial energy and describe the steady state cell shape by minimizing the metabolic potential for different collagen densities. As the gel density increases, the number of ligands available increases and the adhesive energy becomes increasingly negative i.e. γ_1 is higher for high-density collagen matrices. However, as described in SI Section S2.2.6, the membrane tension is two orders of magnitude larger than the energy of receptor-ligand adhesions. Particularly, for mesenchymal cells, it has been observed that the membrane tension is higher on stiffer matrices[48]. Hence, we choose the effective interfacial energy ($\gamma = \gamma_0 - \gamma_1$) to be an increasing function of collagen density, the exact functional form being determined by a sensitivity analysis (see SI Section 2.2.6, Figure S9). When using this form for interfacial energy, the cell shape predicted by minimizing the metabolic potential shows a clear biphasic variation with matrix stiffness (see Figure 5a).

To understand how the metabolic potential dictates cell morphology, we consider the effect of cell elongation and matrix density on the volumetric part of the metabolic potential and interfacial energies, separately. By examining the individual energetic components of the volumetric part of the metabolic potential, we observe that the ATP hydrolysis energy is the most dominant component, as it shows the greatest change from one cell shape to another at any given matrix density (Figure S7). Thus, the shape that minimizes the volumetric part of the metabolic potential is also the one that maximizes ATP consumption and is under maximum cytoskeletal tension. The

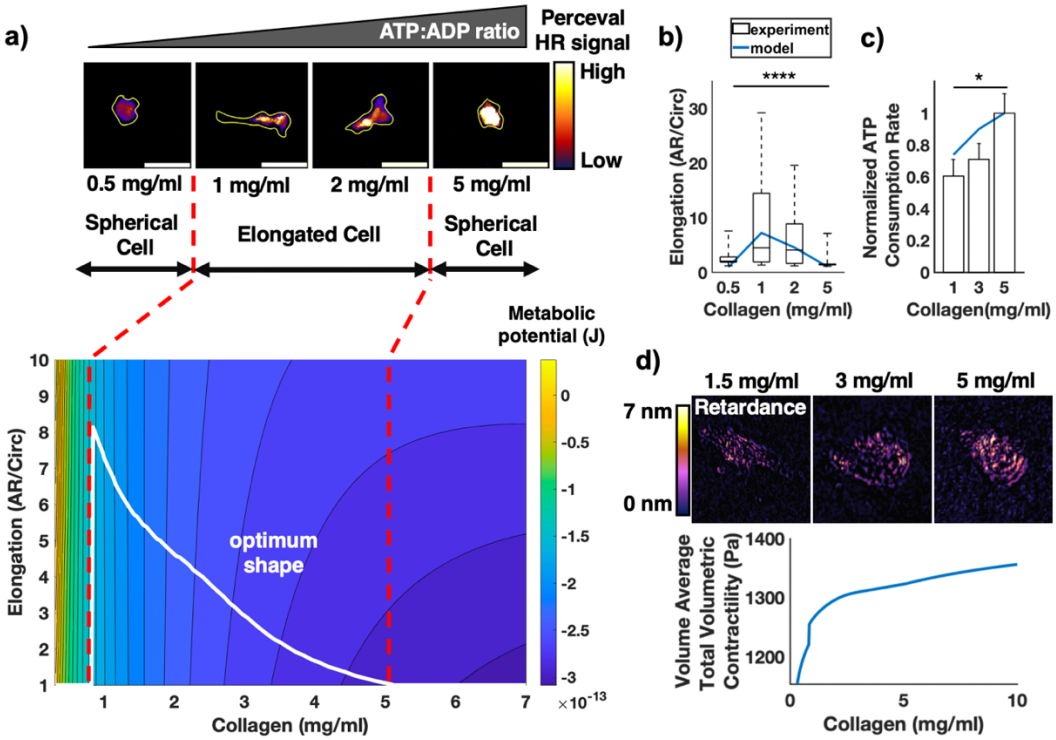

Figure 5: Model predictions of cell shape, ATP consumption, and contractility for mesenchymal cells in 3D collagen networks are in good agreement with experimental data. (a) Contour plot of the metabolic potential as a function of collagen density and cell elongation. Simulation predictions as compared to reported experimental measurements of MDA-MB-231 cells in 3D collagen for cell elongation[17] (b) and normalized ATP consumption rate[54] (c). The experimentally measured optical retardance signal[56], which correlates with contractile strain in cells is displayed in (d) along with model predictions of steady state contractility vs collagen density. Bar plots show mean ±SE, and box plots show median, 25th/75th percentiles, and 5th/95th percentiles *p<0.05, **p<0.01, ***p<0.001, ****p<0.001 with Kruskal-Wallis one-way ANOVA. Scale bar = 50 μm.

interfacial energy of the cell increases as the cell body aspect ratio increases beyond unity (Figure S10). For a given cell aspect ratio, the interfacial energy is higher for denser collagen matrices, however, the change in interfacial energy with elongation is nearly similar for all collagen densities. At low and high collagen densities, our model predicts that the cell adopts a rounded shape, while at intermediate matrix density, it has an elongated shape ($EF > 1$) (see Figure 4a) as we discuss next.

- *Low Collagen Density (<0.5 mg/ml)*: Cells in low density collagen do not generate high magnitudes of cytoskeletal stress, even when they adopt highly elongated shapes (Figure 4a) because the surrounding matrix is too soft to support large stresses. Hence, the stress-regulated enhancement in myosin motor recruitment and consequently the energy available through ATP hydrolysis is low for both spheroidal and elongated configurations (Figure S7). In this case, the decrease in the volumetric part of the metabolic potential as the cell goes from a spheroidal to an elongated shape is also very low and is not sufficient to overcome the increase in interfacial energy (Figure S10) associated with such a shape transition. Hence, our model predicts that the cell adopts a spheroidal shape (Figure 4c) in low density collagen matrices. This agrees with experimental predictions of cell elongation at low collagen densities (Figure 5a-b).
- *Medium Collagen Density (0.5 – 5 mg/ml):* Here, the stresses and consequently the contractility is larger for all cell elongations compared to cells on low collagen density (Figure 4a). Also, the decrease in the volumetric part of the metabolic potential as the cell elongation changes is higher than the corresponding decrease on soft matrices (see Figure S7). This decrease is sufficient to overcome the increase in interfacial energy (Figure S10) and the cell adopts the elongated shape (Figure 4c) at steady state, which compares well with the experimentally observed cell elongation in matrices of intermediate density (Figure 5a-b).
- *High Collagen Density (>5 mg/ml):* While very high stresses and contractility are generated for cells in highly dense collagen matrices (Figure 4a), the decrease in the volumetric part of the metabolic potential with cell elongation is slightly smaller than observed on cells in intermediately dense collagen (Figure S7). This suggests that the decrease in the volumetric part of the metabolic potential achieved with elongation saturates at intermediate values of matrix stiffness. This happens since at high matrix stiffnesses, even spherical cells can generate high levels of stress and contractility. Thus, the associated change in the energy of ATP hydrolysis and the volumetric part of the metabolic potential with elongation is smaller for high-density collagen as compared to medium-density collagen. This difference indicates interfacial energy once again prevents the cell from elongating (Figure S10). Hence, cells adopt a spherical shape on high density collagen (Figure 4c), which is also reported from experiments (Figure 5a-b)

In summary, only in intermediate stiffnesses is the magnitude of contractility as well as the difference in contractility between spherical and elongated cells high enough to overcome the increase in interfacial energy, leading to elongated cell shapes at steady state. Despite the non-monotonic variation in cell shape with collagen density, the volume-averaged cell contractility corresponding to the optimum cell shape monotonically increases with gel density (Figure 5d). The optical retardance signal obtained for MDA MB-231 cells using quantitative polarization microscopy (QPOL)[56] is a measure of the contractile strain on actin in cells and it is seen that for MDA MB-231 cells in 3D collagen, an increase in matrix density is associated with a higher intensity of the optical retardance signal (see Figure 5d), validating our theory. Also, we show that the ATP consumption rate (Eq S2.28) at steady state predicted by our model increases with collagen density (Figure 5c), which underscores the fact that the higher contractility of cells on denser matrices is driven by their tendency to lower metabolic potential. This trend shows good

agreement with the rate of ATP consumption measured experimentally for MDA MB-231 cells as the time-averaged decrease in the PercevalHR signal after treating the cells with antimycin A and iodoacetate, which inhibit OXPHOS and glycolysis, respectively[54] (Figure 5c).

3.2 Minimizing the metabolic potential predicts two distinct morphology transitions with increasing matrix stiffness for cells on 2D substrates

We now consider the steady state cell morphology, contractility, and ATP consumption of MDA-MB-231 cells plated on 2D PA gels. To predict the cell shape and contractility on 2D substrates as a function of matrix stiffness, we use the biophysical parameters of MDA-MB-231 cells determined by iterative analyses performed for cells in 3D collagen (see Table S4 for description and values of parameters used) with no additional fitting parameters. Cells on 2D substrates are modeled as half-ellipsoids with distinct semi-axes, a, b and c as shown in Figure 6c. In general, $a \neq b \neq c$, and the specific case where they are all identical represents a hemispherical cell. To completely characterize the shape of a cell seeded on 2D substrates, we define two aspect ratios- a/b and c/b which represent elongation or contraction along the cell-matrix interface and the direction perpendicular to the cell-matrix interface, respectively (Figure 6c). The cell volume is assumed to be constant and thus the cell spreading area ($A = \pi ab$) scales inversely with the c-axis. Thus, an increase in the cell spread area means that the cell is flattening along the c-axis. While we examined a range of cell shapes, we find that considering the energetic contributions of a particular set of three important shapes is enough to explain the morphologies adopted by cells on 2D substrates. These three shapes are: a) spheroidal ($\frac{a}{b} = 1, \frac{c}{b} = 1$), (b) spindle-like ($\frac{a}{b} > 1, \frac{c}{b} < 1$) and (c) disc-like ($\frac{a}{b} = 1, \frac{c}{b} < 1$) (Figure 6a). Similar to the 3D case, the matrix is modeled as a cylinder with a radius greater than 50 times that of the cell to minimize boundary effects. The mechanical behavior of the matrix is modeled as linear elastic matrix, which represents PolyacrylAmide (PA) gels[57] and the stiffness is varied from 1-200 kPa. A thin layer of collagen is added over the entire surface which represents adhesive ligands that facilitate adhesion between the cell and the ECM.

Unlike cells in 3D collagen networks, cells on 2D substrates have two contributions to the interfacial energy: a) cell-matrix interfacial energy γ^{CM} and b) the energy of the "free" surface of the cell $\gamma_0^c S_c$, where γ_0^c is the surface tension of the free surface of the cell (which is not in contact with the ECM) and similarly S_c is the surface area of the free surface. The cell-matrix interfacial energy, γ^{CM} has two contributions, namely the membrane/cortical tension associated with the cell-matrix interface γ_0^{CM} and the adhesive energy due to interaction between integrins on the cell and ligands on the matrix, γ_1^{CM}. We can write γ^{CM} as $\gamma_{eff}^{CM} S_{CM}$ where S_{CM} is contact area at the cell matrix interface and $\gamma_{eff}^{CM} = \left(\gamma_0^{CM} - \gamma_1^{CM}\right)$ is the effective cell-substrate interfacial tension. Now the overall interfacial energy of the cell-matrix system $\Gamma(\Theta)$can be found by summing the cell-matrix interfacial energy and the energy of the free surface. By combining small-depth AFM indentation experiments with models for the analysis of compression of elastic particles, the surface tension of MSC spheroids (γ^C) was determined to be ~0.7 mN/m [58]. Along the cell-matrix interface, while the local membrane tension near focal adhesions was measured to be of the order of 0.09 mN/m[59], the distance between focal adhesions (~5 μm)[60] is typically larger than the distance over which local perturbations to the membrane tension can propagate, hence the cell-matrix

membrane tension is typically lower than the bulk membrane tension value. Hence, a reasonable order of magnitude estimate for the membrane tension along the cell-matrix interface γ_0^{CM} can be considered to be 0.09 mN/m. As described in SI Section S2.2.6, the energy of integrin-ligand adhesions γ_1^{CM} is of the order of ~0.001 mN/m. We conducted iterative analyses with simulations

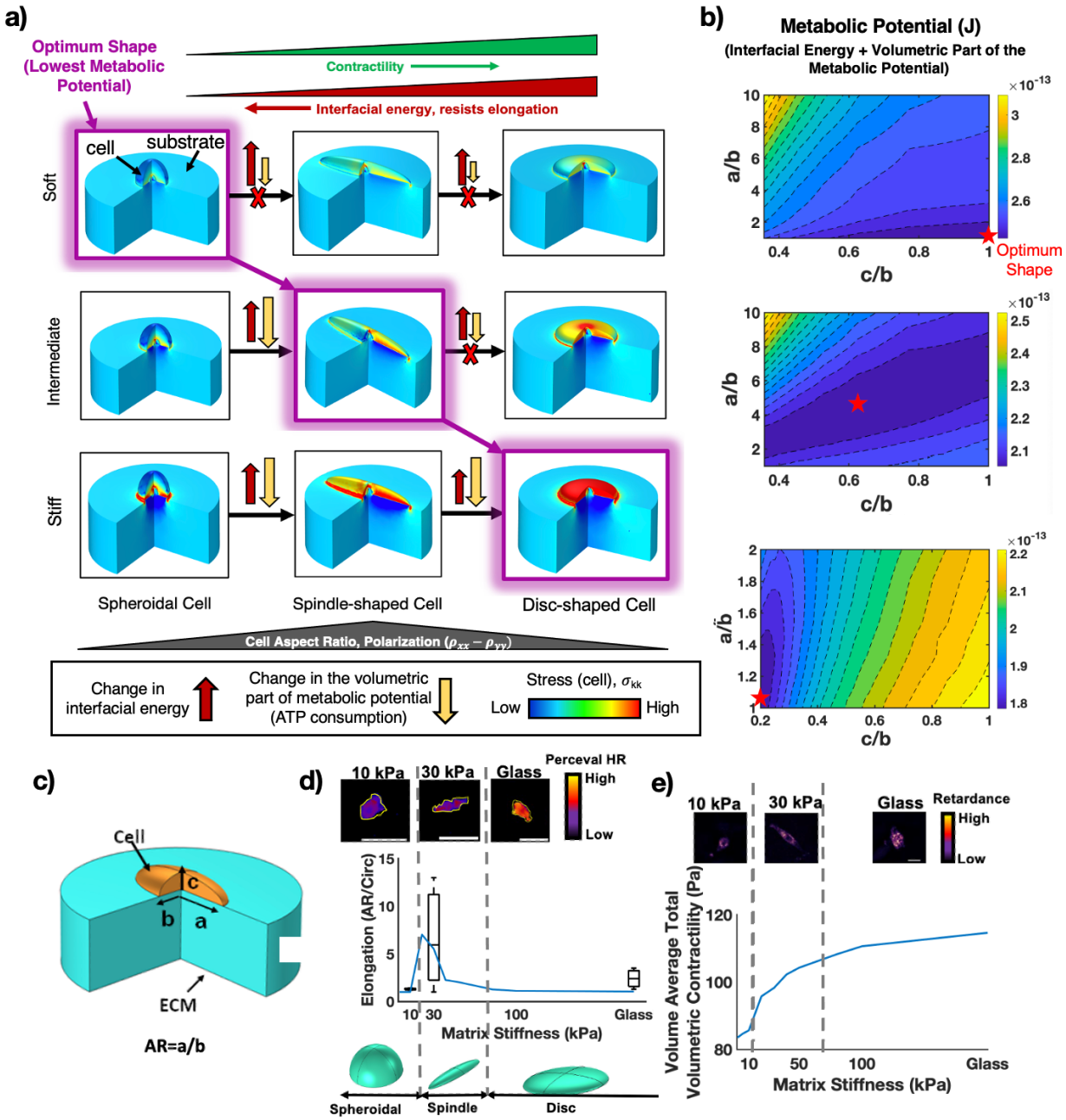

Figure 6: Minimizing the metabolic potential predicts two distinct shape transitions with matrix stiffness for cells in 2D. (a) Optimum cell shape shows a transition from hemispherical on soft gels to spindle-shaped on intermediately stiff PA gels and disc-shaped on stiff gels as determined by the interaction between the volumetric part of the metabolic potential (red block arrows) and the interfacial energy (yellow block arrows). (b) Contour plots of the metabolic potential as a function of the cell aspect ratios a/b and c/b with the optimum cell shape indicated. (c) Schematic depiction of the geometry of a cell on a 2D substrate. Comparison of (d) cell elongation and (e) cell contractility at steady state predicted by the model with the corresponding data from experiments performed with MDA-MB-231 cells seeded on unconfined 2D substrates[17,54]. Box plots show median, 25th/75th percentiles, and 5th/95th percentiles. Scale bar = 50 μm.

of MDA-MB-231 cells on 2D PA gels to determine the values of the surface tension of the free cell surface γ^C, membrane tension along the cell-matrix interface γ_0^{CM} and the integrin-ligand energy γ_1^{CM} at which model predictions of cell morphology show good agreement with experimental measurements[17,56]. These values are listed in Table S4 and fall within the order of magnitude realms observed experimentally and described here.

To determine the steady state cell shape as a function of matrix stiffness, we compute the metabolic potential given in Equation 9 for various combinations of the shape parameters $\Theta = \{\frac{a}{b}, \frac{c}{b}\}$ corresponding to different values of the matrix stiffness. These contours, along with the steady state cell shape found as the shape parameter that corresponds to the minimum in the metabolic potential, are displayed in Figure 6a-b. While simulations have been performed over a range of matrix stiffness values, the trends reported here on the cell shape, polarization, and contractility correspond to the three representative cases of soft, intermediately stiff, and stiff matrices which have Young's modulus values of 10, 30 and 200 kPa, respectively.

3.2.1 Anisotropic cell shapes develop larger cytoskeletal stress and polarized contractility: We define cell polarization as $p = (\rho_{xx} - \rho_{yy})/\rho_0$, where, ρ_{xx} is the contractility along the a-axis (direction of elongation), ρ_{yy} is the contractility along b-axis (see Figure S11a) and ρ_0 is the cell contractility in the quiescent state. As the cell shape changes from hemi-spheroidal to spindle, the stress field is polarized (see Figures 6a, S11c) and promotes enhanced recruitment of myosin motors along the direction of elongation, which in turn increases the overall volume-averaged cytoskeletal stress $(\frac{1}{V_c}\int_{V_c} \sigma_{kk} dV_c)$ experienced by the cell (see Figure S11c) and thereby the cell contractility (Figure S11b). If we examine the spatial distribution of the volumetric stress σ_{kk} along the cell body, we observe that, for any gel stiffness, the model predicts the highest magnitude of stress near the cell-ECM interface for all cell shapes (Figure 6a). Consequently, the cell contractility is significantly higher near the cell-substrate interface for the hemispherical, spindle and disc-shaped cells (see Figure 6a) while it is lower at regions further away from the interface that are free from constraints.

For the disc-shaped cell, the stress decays more gradually away from the cell-matrix interface as compared to the hemi-spherical and spindle-like configurations i.e., while the hemispherical and spindle-like cells can develop high magnitudes of stress only near the cell-ECM interface, the disc-shaped cell can develop more uniformly high stresses across the cell body (Figure 6a), leading to the highest overall volume-averaged cytoskeletal stress among the three configurations at all matrix stiffness levels (Figure S11e). Also, for all matrix stiffness values, the motor density is uniformly high throughout the disc-shaped cell, leading to higher volume-averaged cell contraction (Figure S11d). As a result, the energy available through ATP hydrolysis is highest for the disc-shaped cell (see Figure S12). Similar to cells in 3D collagen, the energy of ATP hydrolysis is the most dominant component of the volumetric part of the metabolic potential, and if we disregard considerations of interfacial energy, this shape will be the optimum shape for all levels of matrix stiffness. However, by considering both the volumetric part of the metabolic potential and interfacial energies (the total metabolic potential), we find that, like cells in 3D collagen matrices, the optimum cell shape on a 2D substrate transitions from hemispherical on soft matrices to spindle-shaped on matrices with intermediate stiffness (Figures 6a and b).

The rationale behind the hemispherical-spindle-disc shape transition is as follows: on soft gels, though the spindle and disc-shaped cells achieve higher stress and contractility than the hemispherical cell, the associated decrease in the volumetric part of the metabolic potential is not sufficient to overcome the increase in interfacial energy (see Figure 6a). Hence, cells adopt a

hemi-spherical steady state configuration on soft substrates (see Figure 6b). On intermediately stiff gels, while the cell contractility increases significantly and is highest for the disc-like cell, it is still not high enough to overcome the high interfacial energy associated with the disc shape, and the spindle-like cell emerges as the optimum configuration (see Figure 6b). However, on stiff matrices, the disc-shaped cell is able to achieve a significantly greater decrease in the volumetric part of the metabolic potential than the spindle shaped cell (Figure 6a) due to higher extent of mechano-signaling and a lower metabolic potential, consequently emerging as the optimum cell shape (Figure 6b). Also, similar to cells in 3D collagen, our model predicts that the steady state contractility increases with matrix stiffness, which agrees with the experimentally measured trends in optical retardance[56], which correlates with contractile strain in actin fibers (Figure 6e). The trends in cell shape predicted by our model show good agreement with the experimental results reported for MDA MB-231 cells (see Figure 6d) cultured on 2D PA gels. The biphasic variation of the cell aspect ratio a/b (Figure 6d) with matrix stiffness, along with the associated increase in cell spread area (see Figure S13), fully captures the spherical-spindle-disc shape transition observed in cells seeded on 2D substrates. In the absence of interfacial energy, the cells adopt the shape that can achieve the maximum contractility, and hence maximize ATP consumption (Figures S11b), similar to cells in 3D collagen (Figure S8b-c). Thus, the steady state configuration adopted by cells is decided by a balance between its propensity to maximize ATP consumption and the energetic cost of adopting anisotropic shapes, imposed by the interfacial energy. In the next section, we will briefly describe a model to calculate the ATP consumed by cells to maintain their steady state configuration and how it varies with stiffness.

3.3 A mathematical framework for predicting mechano-sensitive ATP replenishment

So far, we have shown how our model predicts that cells in stiffer environments develop more contractility and accordingly exhibit larger associated rates of ATP consumption. Here, we seek to elucidate the physical mechanisms that govern ATP production in response to the bio-energetic demands placed on them by stiff micro-environments. We develop a theory for ATP replenishment with the goal of quantitatively predicting important bio-energetic indicators such as ATP levels, ATP:ADP ratio, glucose uptake, and the extent of mitochondrial oxidative phosphorylation as a function of matrix stiffness. We first quantitatively describe the mechanisms that involve ATP consumption in an adherent, contractile cell in response to the micro-environment and then proceed to outline the proposed mechano-sensitive ATP replenishment pathways along with a description of the model parameters that are used to quantify them (refer SI Section 3 for full derivation). Next, we describe briefly, how the model parameters are determined by comparison against previously reported experimental data and validate the choice of parameters by testing model predictions against new experimental measurements of bioenergetics for MDA MB-231 cells we carried out.

3.3.1 Quantitative description of ATP consumption on stiff vs soft micro-environments: All living cells maintain a high, non-equilibrium ratio of ATP to ADP, in the range 1-10[61]. While many cellular processes such as ion transport and substrate phosphorylation consume ATP, as widely reported, in highly contractile cells, actomyosin ATPase accounts for close to 50% of the ATP consumed[62–64]. To describe ATP consumption, we consider the ATP hydrolysis reaction (see reaction (1), Table 1), where k_1^+ and k_1^- are the rate constants that govern ATP consumption and production, respectively. As ATP consumption is primarily due to mechano-sensitive engagement of myosin motors to actin filaments, we assume the reaction rate constant that governs ATP consumption (k_1^+) to depend on the on and off rates governing motor binding and unbinding, which in turn are functions of the cytoskeletal stress. Therefore, we take k_1^+ to depend linearly on the volumetric stress σ_{KK}, as $k_1^+ = r_0\ {\sigma_{KK}}^l$, where r_0 is a proportionality constant, and l is an exponent that

controls the sensitivity of the rate constant governing ATP consumption to stress (Table 1). Thus, once the tensile stress levels are known from the 3D active model we have developed, total ATP consumption rates can be computed by integrating the spatial consumptions rates over the volume of the cell. Higher cytoskeletal tension on stiff substrates is associated with more ATP consumption. Further, ADP can be converted into AMP (reaction (3), Table 1) by loss of an inorganic phosphate group, and the ratio of the reverse (k_2^+) and forward (k_2^-) reaction rate constants, γ' (Table 1) is used to represent this interconversion. Thus, the hydrolysis of ATP leads to a decrease in ATP:ADP ratio, and an associated increase in the AMP:ATP ratio (see Figure 7b).

3.3.2 ATP replenishment through mechano-sensitive calcium mediated AMPK activation: Central to the overall control of cell metabolism is the "master metabolic regulator" AMPK which regulates most of the cells' major catabolic and anabolic pathways including OXPHOS and glycolysis in response to changing cellular energy levels[65]. AMPK is a heterotrimer, comprised of a catalytic subunit AMPKα, and two regulatory sub-units, AMPKβ and AMPKγ. Activation of AMPK (active

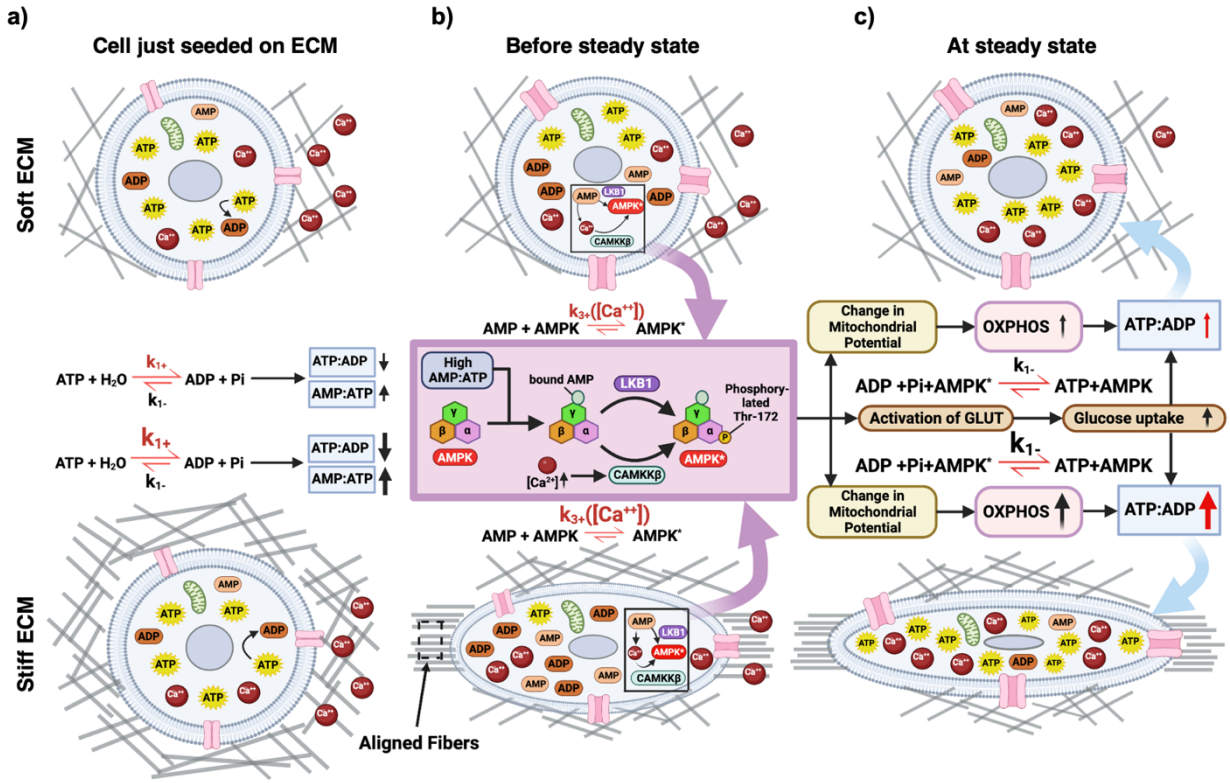

Figure 7: ATP replenishment pathway based on the mechano-sensitive calcium-mediated activation of AMPK. (a-c) Schematic representation of the ATP, ADP and AMP levels (a) immediately after the cell is seeded on an extracellular matrix, (b) before reaching steady state and (c) at steady state for cells in both soft and stiff environments. While the initial metabolic state just after the cell is seeded on the ECM is identical for cells in both the stiff and soft matrices (a), more ATP is consumed by cells on the stiff substrate due to the activation of stress-regulated signaling mechanisms (the Rho-ROCK and Ca^{2+} pathways) that lead to enhanced motor recruitment and more ATP hydrolysis (b). Cells on stiff substrates see a marked increase in intracellular Ca^{2+} levels as compared to the baseline value due to stress-assisted opening of ion channels. Activation of AMPK is mechanosensitive and depends on intracellular Ca^{2+} concentrations (see inset purple box), leading to greater extent of AMPK activation on stiff matrices. At steady state (c), mechanosensitive activation of AMPK has upregulated ATP production such that ATP levels are higher on stiff than soft. Our model captures these mechanisms by taking the rate constant governing the reaction in which AMP and AMPK yield active AMPK, k_3^+, to depend on the concentration of intracellular calcium.

form is written as AMPK*) is a critical step in the replenishment of ATP and is initiated by the allosteric binding of AMP[65] to the AMPKγ subunit. This induces a conformational change in the complex, thereby making the AMPKα subunit a more suitable site for phosphorylation by upstream kinases (Figure 7b). Two kinases, namely LKB1 (liver kinase B1) and CAMKKβ (Ca2+/calmodulin-stimulated protein kinase kinase beta) have been shown to promote phosphorylation of AMP-bound AMPK at Thr-172 (threonine) on the AMPKα subunit (Figure 7b). Higher expression levels of these kinases lead to more AMPK activation. We represent the formation of AMPK* by the chemical reaction (4) in Table 1, such that k_3^+ denotes the rate constant that governs activation of AMPK* and k_3^- is the reverse rate constant. Here, we consider the rate constant governing AMPK activation k_3^+ to be a function of the LKB1 and intracellular calcium levels, to represent the upstream effect of these kinases on AMPK activation.

As energy levels in the cell are depleted, AMP levels increase which leads to higher levels of AMP-bound AMPK. This effect is more pronounced on stiffer substrates (Figure 7a-b). While LKB1 levels are not known to be affected by the stiffness of the micro-environment, it is well established that the intracellular calcium levels are higher on stiffer substrates[66–68]. Particularly, in mesenchymal cells, the higher membrane tension associated with stiffer micro-environments[48,69] directly cause an increase in intracellular calcium levels through the opening of stress-activated ion channels[69,70]. This mechano-sensitivity of calcium signaling is modeled by considering the reaction rate constant that governs AMPK activation, k_3^+, to be an increasing function of cytoskeletal stress ($k_3^+ = k_3^+(\sigma_{kk})$). Also, the reverse rate constant, k_1^- ,which governs ATP synthesis is an increasing function of [AMPK*], which represents upregulation of ATP synthesis by AMPK*. As several upstream signaling pathways mediate activation of AMPK, it is difficult to isolate the effect of cellular stress on AMPK activation through calcium signaling, and we assume the rate constant governing AMPK activation through calcium signaling to depend on the cytoskeletal stress as $k_3(\sigma_{KK}) = {\sigma_{KK}}^m$. The important rate constants and how they depend on various biophysical parameters like the cytosolic calcium level, concentration of AMP and [AMPK*] are summarized in Table 1. To determine the steady state levels of ATP, ADP and AMP, we set the rates of change of the concentration of the nucleotides to zero. Further, we enforce the constraint that the total concentration of the nucleotides is constant and that the sum of non-activated and activated AMPK is also a constant. This leads to a set of five equations that we solve simultaneously to determine the concentrations of the phosphates and the two forms of AMPK at steady state. For a detailed derivation, the reader is referred to the SI section 3.1.

Chemical Reaction	Biophysical parameters that govern reaction rate
(1) $ATP + H_2O \xrightarrow{k_1^+} ADP + P_i + \Delta G^*$	$k_1^+ = f\big(k_{on}(\sigma_{kk})\big) = r_0 \sigma_{kk}^l$
(2) $ADP + P_i \xrightarrow{k_1^-} ATP$	$k_1^- = f_1([AMPK^*]) = r_1[AMPK^*]$
(3) $AMP + P_i \underset{k_2^-}{\overset{k_2^+}{\Leftrightarrow}} ADP$	$\gamma' = \frac{k_2^-}{k_2^+}$
(4) $AMP + AMPK \underset{k_3^-}{\overset{k_3^+}{\Leftrightarrow}} AMPK^*$	$k_3^+ = f_2([AMP], [Ca^{2+}])$

Table 1: Important biophysical parameters in the ATP replenishment model. Here, ΔG^* is the energy released due to hydrolysis of 1 mol of ATP.

3.3.3 Determination of the model parameters: We find that to predict the steady state ATP:ADP ratio as a function of matrix stiffness it is enough to know the following parameters: a) the cytoskeletal stress in fully spread cells as a function of substrate stiffness, b) the intensity of

calcium signaling as a function of matrix stiffness that is represented in our model by the parameter k_3 , and c) the parameters r_0 , r_1, γ' (the ratio of k_2^- to k_2^+), l and m. The cytoskeletal stress in fully spread cells is determined from our model as the volume-averaged stress ($\int \sigma_{KK}\, dV$) corresponding to the optimum configuration found by minimizing the metabolic potential, R, in both 2D and 3D micro-environments, for different substrate stiffness values. We show in SI Section 3.1 how we determine parameter values by fitting model predictions to experimentally measured values of [ATP]:[ADP], and note that our model predicts an increase in the ATP:ADP ratio with collagen density/matrix stiffness for MDA MB-231 cells, as long as $m > l$. Physically, this suggests that the increase in time-averaged intracellular calcium levels is higher than the increase in myosin motor activity for the same increase in stress. This implies that the extent of calcium-mediated AMPK activation and ATP synthesis is higher than the ATP consumed, and cells maintain correspondingly high ATP:ADP ratios at steady state in agreement with experimental observations[14]. The ATP:ADP trends predicted by our theory agree with experimentally measured trends in PercevalHR levels as a function of collagen density/substrate stiffness[17,54] for MDA MB-231 cells, suggesting that calcium-mediated activation of AMPK increases much more rapidly with substrate stiffness than does motor activity, the availability of AMP being the limiting step for AMPK activation. In the next sections, we discuss model predictions of ATP:ADP ratio and [AMPK*] for cells in both 2D and 3D micro-environments and compare it with both existing and new experimental data.

3.4 Cells maintain higher ATP:ADP ratios and activated AMPK levels in stiffer micro-environments

Our theory captures the experimentally observed trends that the ATP:ADP levels increase with collagen density (Figure 8a). We perform a least-squares fitting of Eq. (S3.17) to the experimentally measured ATP:ADP ratios for collagen densities from 0.5 to 5 mg/mL to determine the model parameters (Table S5, Figure S14). To validate the model, we analyze MDA-MB-231 cells in 2D micro-environments using the parameters listed in Table S5, with no additional assumptions. The steady state ATP:ADP ratio for MDA-MB-231 cells on 2D PA gels predicted from our theory shows a monotonic increase with matrix stiffness (Figure 8b), in agreement with experimental measurements for MDA-MB-231 cells plated on PA gels[17]. Despite the cell polarization showing a biphasic variation with increasing matrix stiffness unlike the case of 3D collagen, the steady state ATP:ADP ratio shows a monotonic increase in both 2D and 3D micro-environments, as the optimum configuration adopted by cells on stiff substrates has higher contractility (Figure 5d and 6e), leading to both higher ATP consumption and associated replenishment on stiff substrates.

3.4.1 Model predictions of activated AMPK levels increase with ECM stiffness and correlate with experimentally measured levels of glucose uptake and OXPHOS: Our theory provides a general framework to predict important biophysical parameters and variables, key among them being activated AMPK levels as a function of matrix stiffness. As experimental data pertaining to the direct measurement of [AMPK*] at the single-cell level is not available, we performed experiments to measure [AMPK*] at the single-cell level in cells cultured on both 2D PA gels and in 3D collagen (Figure 8f and 8g). The total immunofluorescence signal calculated from confocal images of MDA-MB-231 cells stained for AMPK phosphorylated at αThr-172 was used to quantify relative amounts of AMPK activation (refer SI Section 3.2 for details). We find significant increases in AMPK activation in stiffer environments both in 3D collagen (Figure 8f) and on 2D PA gels (Figure 8g) in good agreement with the increase in activation predicted by our model (see SI Section 3.4). These findings are also consistent with other reports in the literature that find elevated AMPK activation in response to stiffer substrates on both short (~5 hrs) and long (~24 hrs) culture timescales[72]. Further, we observe strong localization of activated AMPK to the nucleus (Figure

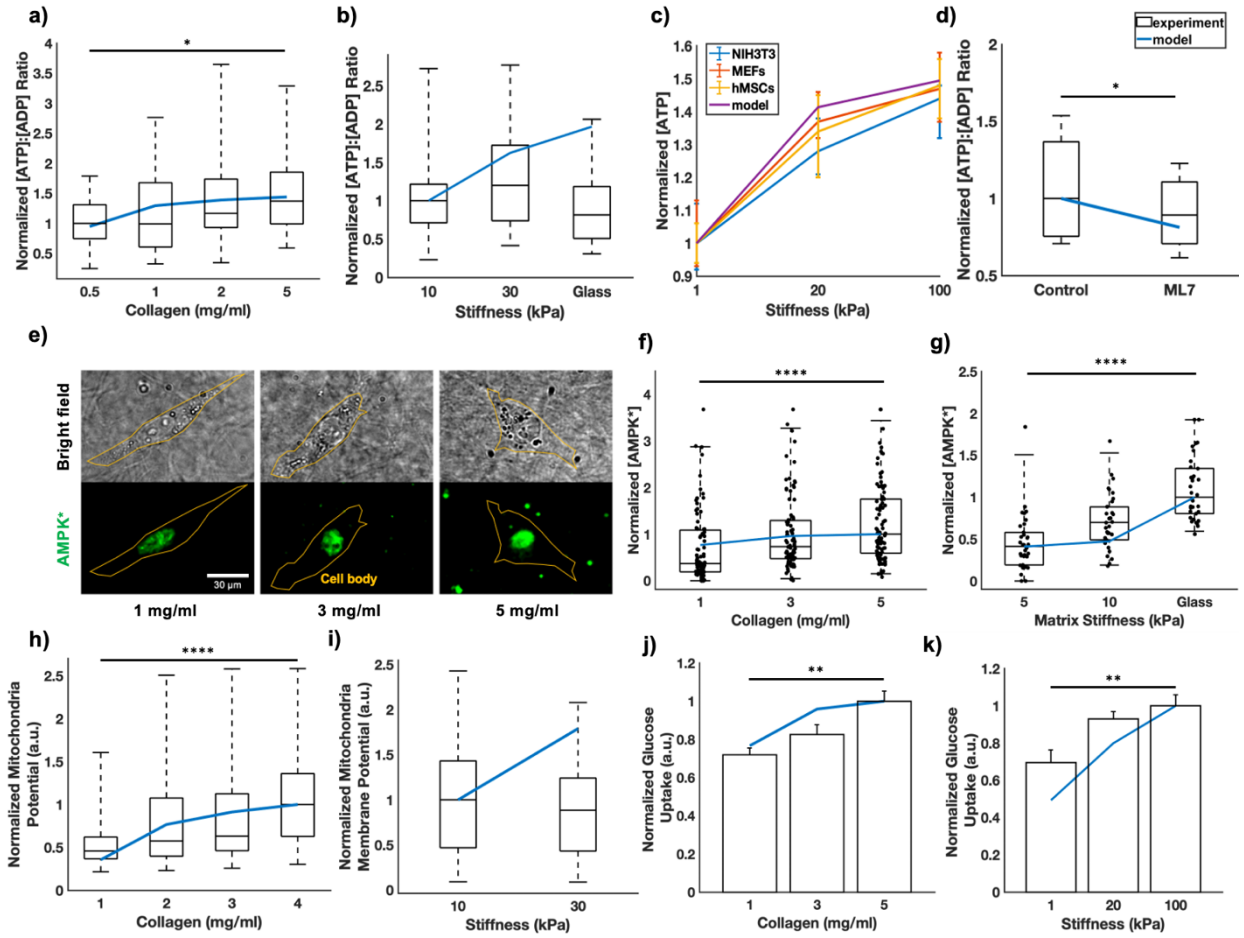

Figure 8: Model predictions of normalized ATP:ADP ratio, ATP levels, [AMPK*] levels and comparison with experimental data. (a) Least Squares fit of steady state ATP:ADP ratio vs. collagen density from theory against experimental measurements of PercevalHR signal[17] to determine model parameters. (b) Model prediction of normalized ATP:ADP ratio for MDA MB-231 cells in 2D using parameters determined from (a) compared with experimental measurements[17]. (c) Model predictions of normalized ATP levels for MDA MB-231 cells compared with experimentally measured ATP levels for hMScs, MEF and NIH3T3 cells[14]. (d) Model prediction of normalized ATP:ADP levels considering myosin recruitment rates (k_{on}) of 2.33kPa^{-1} and 1.5kPa^{-1}, the latter representing the effect of lowered myosin activity compared against experimental measurements for MDA MB-231 cells in 3D collagen of density 1.5 mg/mL treated with ML7 which inhibits MLCK and thereby, the cell's ability to generate contractile forces[54]. (e) Bright field images of MDA MB-231 cells in collagen of density 1, 3 and 5 mg/mL along with corresponding confocal microscopy images of cells stained with phosphorylated AMPK antibody. Model predictions of [AMPK*] as a function of collagen density/gel stiffness compared with experimentally measured relative levels of [AMPK*] (quantified for each cell as the total fluorescence signal using ImageJ software) for MDA MB-231 cells (f) in 3D collagen (n=83) and (g) on 2D PA gels (n=34). Model predictions of [AMPK*] are compared with the reported change in mitochondrial potential for MDA MB-231 cells in (h) 3D collagen and (i) 2D PA gels[17] as well as with glucose uptake levels for MDA MB-231 cells in 3D collagen[54] (j) and hMSCs on 2D gels[14] (k). Bar and line plots show mean ±SE, and box plots show median, 25th/75th percentiles, and 5th/95th percentiles *p<0.05, **p<0.01, ***p<0.001, ****p<0.001 with Kruskal-Wallis one-way ANOVA.

8e), which is consistent with its known role as a transcription factor[71,72]. We also find that our model predictions of increased AMPK activation in stiffer micro-environments strongly correlate with the increased glucose uptake (Figures 8j-k) and change in mitochondrial potential (an indicator of higher OXPHOS rates in cell mitochondria, (Figures 8h-i)), measured experimentally for mesenchymal cells[17,54] in both 2D and 3D micro-environments. To further assess the ability of our model, we compared model predictions of the steady state ATP levels on 2D PA gels to experimental measurements for other mechanosensitive cell types. We find that our model

prediction of the change in ATP (and hence glucose uptake) with matrix stiffness is representative of cell metabolism across various mesenchymal cell types (Figure 8c)[14].

3.4.2 Pharmocological Inhibition of mysoin activity leads to smaller steady state ATP:ADP ratios: To directly predict the effect of inhibiting myosin activity in our model, we simulate MDA MB-231 cells in 3D collagen with a reduced sensitivity toward stress for the kinetic constant governing motor binding k_{on} , while maintaining the other biophysical constants at the same values as listed in Table S4. A smaller value of k_{on} means that myosin motor engagement is lower, even in dense collagen gels, which results in lower levels of cytoskeletal stress (Figure S15). Thus, the rate constant governing ATP consumption k_1^+, which depends on cytoskeletal stress (Table 1), is now smaller, leading to lower ATP consumption. Further, since stress-regulated intracellular calcium levels are also lower, the reaction rate constant governing AMPK activation k_3 is also now smaller, and our theory predicts a lower extent of ATP replenishment. Hence, we expect the steady state ATP:ADP ratio to be smaller for this case. We consider collagen density of 1.5 mg/mL in our simulations, which represents gels of intermediate stiffness. For the same gel density, the contractility, which correlates with the number density of engaged motors, is lower, leading to overall lower cytoskeletal tension. Using Eq. (S3.17), we predict the steady state ATP:ADP ratio for the cells with reduced k_{on} to be smaller (Figure 8d). Inhibition of myosin light chain activity (MLCK) by treating MDA MB-231 cells in 3D collagen (density 1.5 mg/mL) with ML7 is reported to have a similar effect and our model predictions show good agreement with the ATP:ADP ratio measured after inhibition using PercevalHR[54] (Figure 8d).

3.5 ATP:ADP ratio and OXPHOS rate is higher for more elongated cells and cells with larger spread area on 2D substrates

Next, we predict the normalized ATP:ADP ratio as previously measured in MDA-MB-231 cells cultured on 2D micropatterned PA gels[17]. By tailoring the micropattern, cells spreading can be confined to a predetermined fixed area or can be forced to adopt increasingly elongated aspect ratios. For both cases, the cellular energy level as a function of cell elongation and spread area was measured by using the PercevalHR ratiometric reporter to measure ATP:ADP ratio. On PA gels of stiffness 10 and 30 kPa, we consider: a) cells with fixed elongation $(AR/circ \sim 1)$ and (b) cells with fixed area, where the ATP:ADP ratio as a function of increasing cell spread area or cell elongation are computed. To model confined cell spreading, we considered MDA MB-231 cells (properties listed in Table S4) coated on rectangular micropatterns with side lengths a and b, respectively. First, by holding the cell elongation fixed at unity, we vary the rectangular micropattern area and determine the steady state cell contractility, strain and cytoskeletal stress by solving Equations 6 and 7 at every integration point (see SI section 3.4.4 for details). Then we determine the volume-averaged cytoskeletal stress $\frac{1}{V_c}\int_0^{V_c} \sigma_{kk}\, dV_c$ as a function of cell spread area and use it to determine the steady state ATP:ADP ratio (Eq S3.17) as a function of cell spread area. Similarly, we hold the cell spread area constant and determine the volume-averaged cytoskeletal stress as a function of cellular elongation. While we use the same values for the biophysical parameters c and γ as determined from the 3D case (Table S5), we employ a slightly higher value for the stress-sensitivity parameter l, which reflects the higher sensitivity of myosin motor activity to stress during confined cell spreading. Further, let us denote the stress components along the base lengths a and b as σ_a and σ_b, respectively.

Our model predicts that with increasing cell spread area (while holding the elongation constant), the ATP:ADP ratio increases (Figure S16a). Micropatterns that confine cell elongation can be thought of as restricting the cell to shapes that are more hemispherical in nature, and as the cell spread area increases, there is equiaxial recruitment of myosin motors along both base lengths

a and b , leading to a more isotropic increase in stress i.e. both σ_a and σ_b increase by the same levels (as cell area increases) and remain equal in magnitude (σ_a= σ_b), contributing equally to the overall increase in the volumetric cytoskeletal stress σ_{kk}. This is associated with higher ATP consumption and consequent replenishment (Figure S16b). By contrast, for cells confined to a fixed area, more myosin motors are recruited along the elongated axis (a) leading to higher stress along the direction of elongation i.e. σ_a> σ_b, and a consequent increase in ATP consumption and replenishment. Accordingly, our model predicts that the ATP:ADP ratio increases with cell elongation (Figure 9a).

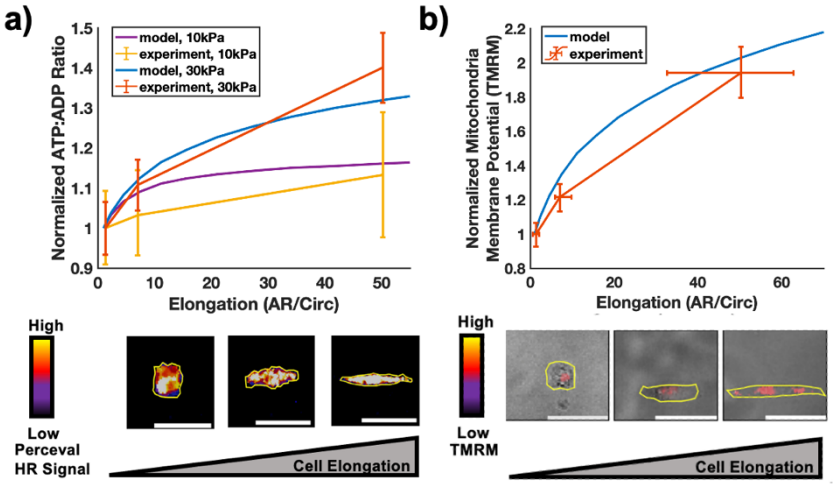

Figure 9: Model predictions of normalized ATP:ADP ratio and activated AMPK levels for cells on 2D PA gels spreading in a confined manner. Comparison of the normalized ATP:ADP ratio predicted by theory with experimental values obtained for MDA-MB-231 cells spreading on collagen micro-patterns[17] at fixed cell spread area (a), considering PA gel stiffness of 10 and 30 kPa and the corresponding concentration of activated AMPK compared with change in mitochondrial potential (TMRM) are shown in (b). Plots show mean ±SE. Scale bar = 50 μm.

Furthermore, for the same increase in elongation, cells on stiffer matrices achieve a higher level of steady state ATP:ADP ratio (Figure 9a) due to the additional effect of increased substrate stiffness promoting the development of higher cytoskeletal stresses and more activation of mechanosensitive pathways that upregulate contractility. We also compare model predictions of the extent of AMPK activation that occurs when cells are allowed to elongate or to experimentally measured mitochondria membrane potentials (Figure 9b). Our model predicts that the concentration of activated AMPK will increase with both spread area (Figure S16b) and cell elongation (Figure 9b) owing to increased signaling due to enhanced contractility in both scenarios. All these model predictions show good agreement with experimental results reported for MDA MB-231 cells[17] (Figure 9a-b) and serve to further validate the proposed model for ATP replenishment in a context where cell activities other than establishment of long-term contractility, such as migration, cannot contribute to observed differences in energy levels.

Discussion

In this study, we developed a non-equilibrium chemo-mechanical model for adherent cells and elucidated the role of mechanosensitive signaling on cell metabolism and changes in morphology and contractility in response to the stiffness of the extracellular microenvironment (Figure 10). We proposed the concept of a “metabolic potential” as the sum of myosin binding energy, motor work, strain energy, energy of ATP hydrolysis and the interfacial energy (Figure 2b). Next, we

demonstrated that the contractility and strain fields generated by minimizing this metabolic potential (Section 2.1.4) are equivalent to the steady state fields predicted by considering the kinetics of mechano-sensitive stress fiber assembly (Section 2.1.2), consistent with the Second Law of Thermodynamics. We showed that by minimizing the metabolic potential with respect to contractility, strain and a shape factor, we can predict the steady state cell shape and contractility as a function of matrix stiffness. We first showed, by considering the example of a cell adhered to microposts (Figure 1a), that the enhanced kinetics of stress fiber assembly and consequent ATP consumption lowered the metabolic potential of cells on stiff posts compared to soft (Figure 1b). Despite the higher strain energy of cytoskeletal and post deformation in stiffer micro-environments and the penalty associated with increasing myosin density from its quiescent level, larger magnitude of energy released by ATP hydrolysis was found to favor more contractile cells on stiff

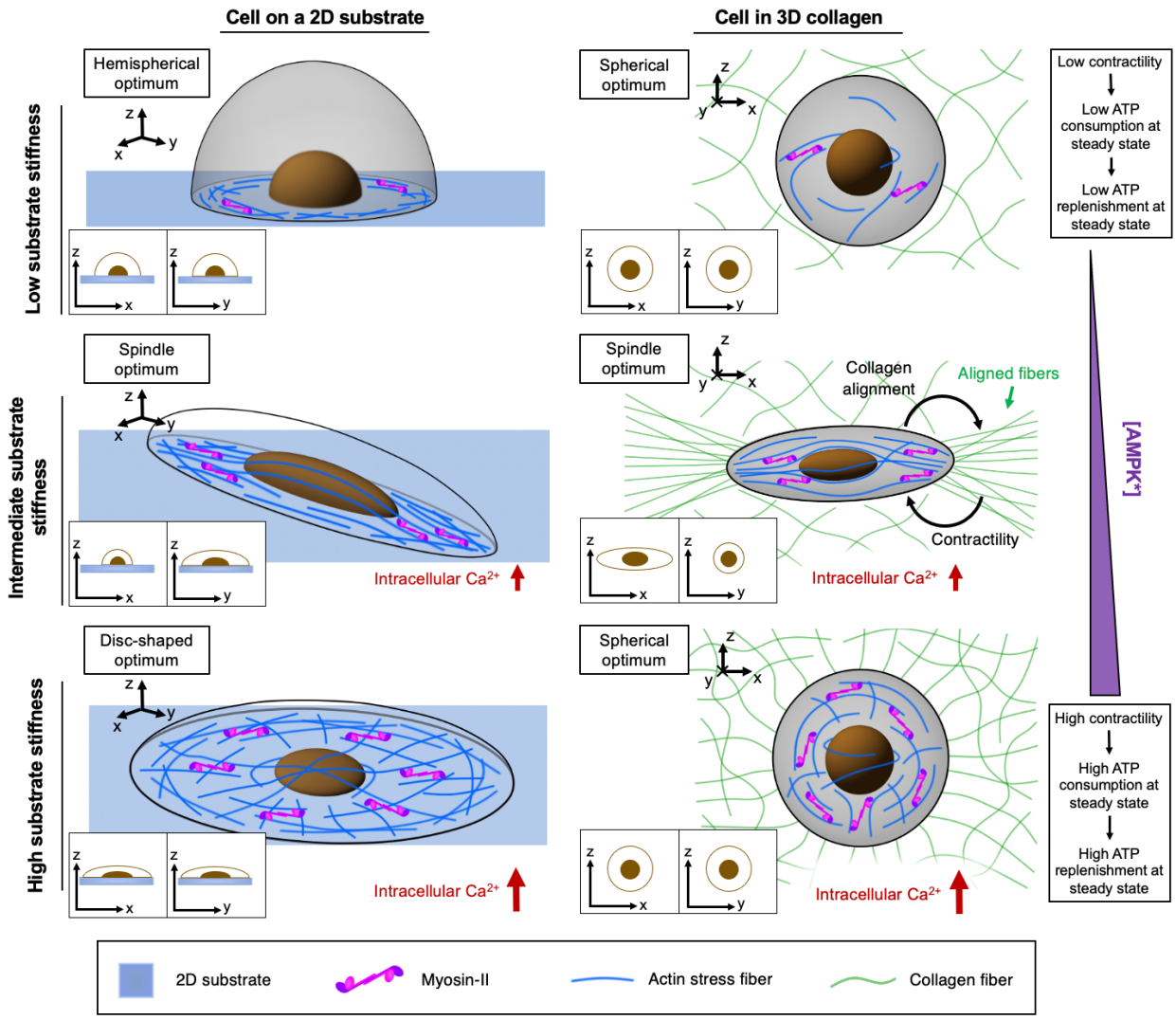

Figure 10: A model to predict how cell shape, contractility, and metabolic regulation depend on mechanosensitive regulation of myosin activity in adherent cells. Cell shape and ECM stiffness determine the distribution and magnitude of stresses generated in an adherent cell which, through mechanosensitive pathways, regulate myosin motor activity and establishment of stress fibers. The decrease in energy achieved by coupling the ATP hydrolysis with stress fiber assembly drives the cell towards a more contractile state and to adopt morphologies that maximize ATP consumption and minimize interfacial energy. Simultaneously, the same mechanosensitive pathways upregulate cytosolic calcium levels which leads to the activation of AMPK through a calmodulin mediated pathway, replenishing cellular ATP stores.

substrates. The model predictions of the contractile force exerted by cells on the microposts was found to scale with the post stiffness (Figure S3b) and showed good agreement with experimental measurements of force exerted by myoblasts on a deformable cantilever arm[34,42]. Using the metabolic potential, we predicted the shape, contractility, and ATP consumption of MDA MB-231 cells (i) encapsulated in 3D collagen and (ii) seeded on 2D PA gels as a function of the stiffness of the micro-environment. For both these cases, we showed that elongated cells will display more contractility and polarized motor activity leading to decreased metabolic potential. However, the interfacial energy between the cell membrane and matrix increases with cell elongation, penalizing anisotropic cell shapes. We showed that the interplay between these competing energies leads to the formation of a minimum in the metabolic potential of the cell, and by finding this minimum with respect to contractility, strain, and the cell body aspect ratio, we identified the optimum shape of the cell body.

Our model reveals that cells encapsulated in a 3D collagen matrix show a distinct biphasic variation in elongation with collagen density (Figure 4a). While the cell remains spherical in both low- and high-density collagen, for intermediate densities, it adopts an elongated shape. In low density collagen, the actomyosin activity of cells is low, even for highly elongated cells, and the metabolic potential is dominated by the interfacial energy. Hence, our model predicts that cells remain spherical on low density collagen to minimize the interfacial energy. For medium density collagen, our model predicts an increase in the actomyosin mediated contractility particularly for elongated cell shapes. This drives the cell body to adopt an elongated configuration for which the associated decrease in the volumetric part of the metabolic potential is higher than the increase in the interfacial energy. In high density collagen, the contractility is uniformly high for all cell body elongations, and the lowering of the volumetric part of the metabolic potential with elongation is consequently insignificant. Hence cells adopt a spherical configuration to minimize the interfacial energy.

Our model predictions agree with the cell body shapes reported for MDA-MB-231 cells as a function of collagen density[17] as well as with similar observations reported for fibroblasts[73] (Figures 5a-b). We showed that the steady state configuration predicted by our model is always more contractile in denser collagen. This correlates well with the optical retardance measured in MDA-MB-231 cells in different collagen densities using quantitative polarization microscopy (QPOL), which utilizes the birefringent properties of actin[57] to provide a direct measure of the contractile strain in the cytoskeleton (Figure 5d). In addition, increased fiber alignment was observed in highly dense collagen matrices[44,53] suggesting significant matrix remodeling activity, which further reinforces the idea that cells are, in fact, highly contractile on stiff substrates. However, it should be noted that when cells lack the ability to degrade the matrix, cellular traction, contractility, and formation of adhesions is suppressed, as reported for hMScs encapsulated in covalently crosslinked hydrogels[74]. This same phenomenon may be observed for MDA MB-231 cells when in very high-density collagen matrices, but likely will not play a role in observed cell behavior at the intermediate collagen densities considered here ($\leq$ 6 mg/ml). Further, our model predicts the deformation energy stored in the collagen matrix due to contractile forces exerted by MDA MB-231 cells to be of the order of 0.03-0.07pJ, which is in good agreement with experimental measurement of the strain energy of these cells measured as the deformation energy released 30 min after treatment with cytochalasin D[75] (Figure S17a).

We showed that cells on 2D substrates also displayed a similar non-monotonic variation in shape and polarization with increase in matrix stiffness. While cells adopted a hemispherical shape on soft PA gels, on gels of intermediate stiffness they adopted elongated spindle-like shapes, and on glass, they were found to adopt a flat disc-like configuration. The disc-like configuration was shown to have lower active energy as compared to the hemispherical and spindle-like shapes, as

the disc geometry was able to develop higher levels of stress throughout the cell body. This effect is most pronounced on stiff PA gels, where the disc shape achieves the lowest metabolic potential and is the predicted optimum cell shape. This agrees with the data reported for fully spread MDA-MB-231 cells on PA gels[17,56]. Similar to cells in 3D collagen, the contractility of the steady state configuration increases with matrix stiffness, which again correlates with retardance measurements reported for these cells[56]. Also, the matrix strain energy predicted by our model for cells on 2D gels is of the order of 0.005-0.01 pJ which is in good agreement with experimental measurements using Traction Force Microscopy for human vein umblical endothelial cells (HUVEC)[76] (Figure S17b). To understand why the strain energy of linear elastic PA gels is lower than collagen gels, we consider the following: collagen fibers stiffen along the direction of applied principal tensile stretch[53] which can facilitate long range force transmission in non-linearly elastic matrices. For a cell contracting in a fibrous matrix, the force in the matrix was found to persist at distances that were several times the cell diameter[53,77], and this larger interaction field could account for the higher matrix strain energy experienced by 3D collagen matrices as compared to PA gels.

Importantly, we developed a model for ATP replenishment based on mechanosensitive activation of AMPK that can predict the steady state levels of ATP, ADP, and activated AMPK as a function of cytoskeletal stress or matrix stiffness (Figure 7). It is well known that the activation of AMPK is essential to trigger ATP synthesis through OXPHOS or glycolysis[65]. Here, we showed that intracellular calcium could be an important regulator of AMPK activation in response to mechanical cues from the matrix. Many studies report an increase in intracellular calcium levels on stiff substrates[66,67,78], and this calcium signaling can trigger the calmodulin-assisted formation of activated AMPK and upregulate both OXPHOS and glycolysis ensuring that the higher energy demand from myosin motor activity on stiffer substrates is always met. We conducted experiments to directly measure activated AMPK levels for both cells in 3D collagen (Figure 8f) and cells seeded on 2D PA gels (Figure 8g). Our model predicts higher concentrations of activated AMPK on stiffer/dense substrates, which is in agreement with our experimental measurements, validating our theory of calcium-mediated AMPK activation. Further, as we discuss below, we also compared our model predictions of ATP, ADP and activated AMPK levels to different experimental measurements to determine if our model can accurately capture observed trends in cell energetics.

It has been reported using PercevalHR measurements that the ATP:ADP ratio of fully spread cells is higher on stiff substrates[17,54]. This is due to the increased OXPHOS and glycolytic activity of cells on stiffer substrates to meet the higher energy demand associated with remodeling stiffer/denser ECM. Indeed, inhibiting OXPHOS activity by treatment with AMA was found to significantly decrease cell elongation, as well as the ATP:ADP levels in these cells, particularly in very dense matrices[17]. Similarly, glucose uptake was found to be higher in fully spread cells in highly dense collagen as compared to low density matrices[54], suggesting that ATP replenishment through OXPHOS and glycolysis is important to establish and maintain cytoskeletal contractility and is modulated by the mechanical properties of the cell micro-environment. We show that our model can capture these reported trends for cells in both 3D (Figure 8a) and 2D (Figure 8b) environments and predict a steady-state ATP:ADP ratio that increases with matrix stiffness. Further, we showed our model for cells seeded on micropatterned PA gels of a fixed stiffness predicts that the ATP:ADP ratio increases when either the elongation or cell spread area is increased independently in good agreement with reported experimental results (Figure 9a-b). These are both scenarios where our model predicts increased contractility and ATP consumption because the cell can develop larger stresses upon spreading or elongating. Hence, the model accurately predicts the fact that the cell tailors its energy production to meet the energy demands imposed on it due to cytoskeletal reorganization in confined environments. Here we assume that

the differences in ATP consumption and hence in AMPK activation between stiff and soft systems is chiefly due to differences in cytoskeletal contractility. This idea is reinforced by experiments where pharmacological inhibition of myosin light-chain (MLC) kinase lead to lower ATP:ADP ratio, suggesting lower AMPK activation[54]. This correlates with our model predictions (Figure 8d) considering suppressed kinetic parameters, further reinforcing the idea that as contractility is inhibited, the cell's energy demands are lower and hence energy replenishment pathways are not triggered.

Further, as we have shown in the Supplementary Section 2.2.3, all the ATP consumed is dissipated as heat at steady state. As there is no net addition of engaged myosin motors at steady state and consequently no change in the conservative energy of the cell, the steady state rate of heat dissipation (Eq. (S2.28)) is a measure of the maximum power that can be generated by the cell. The steady state power calculated for a cell encapsulated in a collagen matrix of density 4mg/mL (which is representative of physiological ECM stiffness) is found to be 2.5 fW (considering a cell volume of 5000 μm^3 as listed in Table S4), while similar calculations for cells on PA gel of stiffness 80kPa yields around 0.9fW. It should also be noted that 1 femtoWatt of power is roughly equivalent to 20,000 ATP molecules consumed per second[35] (see Table S2 to find the list of parameter values used to find the cell power). Thus, we predict that ~50000 ATP molecules are consumed by the cell per second to maintain its steady state configuration. The power generated by myoblasts calculated by measuring the force exerted by them against a deformable plate and the velocity of shortening of the cell was found to be in the range of 0.1-0.5 fW[42]. The power generated by myoblasts is a measurement of mechanical power as the cell contracts and shows good agreement with our model predictions of cells on 2D PA gels. Further, the cell power is higher on denser matrices with cells in low density collagen (~0.5 mg/mL) dissipating only 0.2 fW, which is one-tenth of the power generated on high density collagen (2.5 fW in 4 mg/mL), reinforcing the idea that cells consume more ATP on stiffer/denser matrices.

Understanding the role of mechanical cues in modulating energy production has important implications, particularly, in metastasis of cancer cells. It has been shown that, depending on the stiffness of the micro-environment, either OXPHOS or glycolysis can play an essential role in promoting tumor metastasis and membrane activity in cancer cells. Hence, it is vital to assess how matrix stiffness affects energy production in cells. While we have restricted attention in this study to predicting the steady state energetics of cells in response to matrix stiffness, the ideas presented here can be extended to dynamic processes such as cell spreading and migration, which will be the focus of future work.

Acknowledgements

This work was supported by NIH Award U54CA261694 (V.B.S.); NCI Awards R01CA232256 (V.B.S.); NSF CEMB Grant CMMI-154857 (V.B.S.); NSF Grants MRSEC/DMR-1720530 and DMS-1953572 (V.B.S.); NIBIB Awards R01EB017753 and R01EB030876 (V.B.S.).

References

1. Discher, D. E., Janmey, P. & Wang, Y. Tissue Cells Feel and Respond to the Stiffness of Their Substrate. *Science (1979)* **310**, 1139–1143 (2005).
2. Nagayama, M., Haga, H., Takahashi, M., Saitoh, T. & Kawabata, K. Contribution of cellular contractility to spatial and temporal variations in cellular stiffness. *Exp Cell Res* **300**, 396–405 (2004).

3. Jain, N., Iyer, K. V., Kumar, A. & Shivashankar, G. V. Cell geometric constraints induce modular gene-expression patterns via redistribution of HDAC3 regulated by actomyosin contractility. *Proc Natl Acad Sci U S A* **110**, 11349–11354 (2013).
4. Sonam, S., Sathe, S. R., Yim, E. K. F., Sheetz, M. P. & Lim, C. T. Cell contractility arising from topography and shear flow determines human mesenchymal stem cell fate. *Sci Rep* **6**, 1–12 (2016).
5. Griffin, M. A., Sen, S., Sweeney, H. L. & Discher, D. E. Adhesion-contractile balance in myocyte differentiation. *J Cell Sci* **117**, 5855–5863 (2004).
6. Park, J. S. *et al.* Mechanical regulation of glycolysis via cytoskeleton architecture. *Nature* **578**, 621–626 (2020).
7. Kusakabe, T., Motoki, K. & Hori, K. Mode of Interactions of Human Aldolase Isozymes with Cytoskeletons. *Arch Biochem Biophys* **344**, 184–193 (1997).
8. Wang, J., Morris, A. J., Tolan, D. R. & Pagliaro, L. The molecular nature of the F-actin binding activity of aldolase revealed with site-directed mutants. *Journal of Biological Chemistry* **271**, 6861–6865 (1996).
9. Hu, H. *et al.* Phosphoinositide 3-Kinase Regulates Glycolysis through Mobilization of Aldolase from the Actin Cytoskeleton. *Cell* **164**, 433–446 (2016).
10. Romani, P. *et al.* Extracellular matrix mechanical cues regulate lipid metabolism through Lipin-1 and SREBP. *Nat Cell Biol* **21**, 338–347 (2019).
11. Bertolio, R. *et al.* Sterol regulatory element binding protein 1 couples mechanical cues and lipid metabolism. *Nat Commun* **10**, 1–11 (2019).
12. Helle, S. C. J. *et al.* Mechanical force induces mitochondrial fission. *Elife* **6**, 1–26 (2017).
13. Tharp, K. M. *et al.* Adhesion-mediated mechanosignaling forces mitohormesis. *Cell Metab* **33**, 1322-1341.e13 (2021).
14. Xie, J., Bao, M., Hu, X., Koopman, W. J. H. & Huck, W. T. S. Energy expenditure during cell spreading influences the cellular response to matrix stiffness. *Biomaterials* **267**, (2021).
15. Koo, J. H. & Guan, K. L. Interplay between YAP/TAZ and Metabolism. *Cell Metab* **28**, 196–206 (2018).
16. Via, G. & Signaling, M. Stiffer Matrix Accelerates Migration of Hepatocellular Carcinoma Cells through Enhanced Aerobic. *Cancers (Basel)* **12**, 490–505 (2020).
17. Wu, Y., Zanotelli, M. R., Zhang, J. & Reinhart-King, C. A. Matrix-driven changes in metabolism support cytoskeletal activity to promote cell migration. *Biophys J* **120**, 1705–1717 (2021).
18. Hardie, D. G. AMP-activated protein kinase-an energy sensor that regulates all aspects of cell function. *Genes Dev* **25**, 1895–1908 (2011).
19. Tan, M. J. *et al.* Antidiabetic Activities of Triterpenoids Isolated from Bitter Melon Associated with Activation of the AMPK Pathway. *Chem Biol* **15**, 263–273 (2008).
20. Ceddia, R. B. *et al.* Globular adiponectin increases GLUT4 translocation and glucose uptake but reduces glycogen synthesis in rat skeletal muscle cells. *Diabetologia* **48**, 132–139 (2005).
21. Marsin, A. S. *et al.* Phosphorylation and activation of heart PFK-2 by AMPK has a role in the stimulation of glycolysis during ischaemia. *Current Biology* **10**, 1247–1255 (2000).
22. Marsin, A. S., Bouzin, C., Bertrand, L. & Hue, L. The stimulation of glycolysis by hypoxia in activated monocytes is mediated by AMP-activated protein kinase and inducible 6-phosphofructo-2-kinase. *Journal of Biological Chemistry* **277**, 30778–30783 (2002).
23. O'Neill, H. M., Holloway, G. P. & Steinberg, G. R. AMPK regulation of fatty acid metabolism and mitochondrial biogenesis: Implications for obesity. *Mol Cell Endocrinol* **366**, 135–151 (2013).

24. Horman, S. *et al.* Activation of AMP-activated protein kinase leads to the phosphorylation of elongation factor 2 and an inhibition of protein synthesis. *Current Biology* **12**, 1419–1423 (2002).
25. Kim, J., Kundu, M., Viollet, B. & Guan, K. L. AMPK and mTOR regulate autophagy through direct phosphorylation of Ulk1. *Nat Cell Biol* **13**, 132–141 (2011).
26. Eble, J. A. & Niland, S. The extracellular matrix in tumor progression and metastasis. *Clin Exp Metastasis* **36**, 171–198 (2019).
27. Spill, F., Reynolds, D. S., Kamm, R. D. & Zaman, M. H. Impact of the physical microenvironment on tumor progression and metastasis. *Curr Opin Biotechnol* **40**, 41–48 (2016).
28. Hanahan, D. & Weinberg, R. A. Hallmarks of Cancer: The Next Generation. *Cell* **144**, 646–674 (2011).
29. Conti, M. A. & Adelstein, R. S. Nonmuscle myosin II moves in new directions. *J Cell Sci* **121**, 11–18 (2008).
30. Vicente-Manzanares, M., Ma, X., Adelstein, R. S. & Horwitz, A. R. Non-muscle myosin II takes centre stage in cell adhesion and migration. *Nat Rev Mol Cell Biol* **10**, 778–790 (2009).
31. Katoh, K. *et al.* Rho-Kinase-Mediated Contraction of Isolated Stress Fibers*. The Journal of Cell Biology* vol. 153 http://www.jcb.org/cgi/content/full/153/3/569 (2001).
32. Sit, S. T. & Manser, E. Rho GTPases and their role in organizing the actin cytoskeleton. *Journal of Cell Science* vol. 124 679–683 Preprint at https://doi.org/10.1242/jcs.064964 (2011).
33. Matthews, B. D. *et al.* Ultra-rapid activation of TRPV4 ion channels by mechanical forces applied to cell surface β1 integrins. *Integrative Biology* **2**, 435–442 (2010).
34. Shenoy, V. B., Wang, H. & Wang, X. A chemo-mechanical free-energy-based approach to model durotaxis and extracellular stiffness-dependent contraction and polarization of cells. *Interface Focus* **6**, (2016).
35. Milo, R., and Phillips, R.. Cell biology by the numbers, Garland Science (2015).
36. Kohama, K., Ye, L.-H., Hayakawa, K. & Okagaki, T. Myosin light chain kinase: an actin-binding protein that regulates an ATP-dependent interaction with myosin. *Trends Pharmacol Sci* **17**, 284–287 (1996).
37. Ma, X. *et al.* Ablation of Nonmuscle Myosin II-B and II-C Reveals a Role for Nonmuscle Myosin II in Cardiac Myocyte Karyokinesis. *Mol Biol Cell* **21**, 3952–3962 (2010).
38. Ly Ková Cs* † ‡, M., Thirumurugan, K., Knight, P. J. & Sellers, J. R. *Load-Dependent Mechanism of Nonmuscle Myosin 2*. www.pnas.org/cgi/content/full/ (2007).
39. Schiffhauer, E. S. *et al.* Mechanoaccumulative Elements of the Mammalian Actin Cytoskeleton. *Current Biology* **26**, 1473–1479 (2016).
40. Schiffhauer, E. S. *et al.* Myosin IIB assembly state determines its mechanosensitive dynamics. *Journal of Cell Biology* **218**, 895–908 (2019).
41. Fu, J. *et al.* Mechanical regulation of cell function with geometrically modulated elastomeric substrates. *Nat Methods* **7**, 733–736 (2010).
42. Mitrossilis, D. *et al.* Single-cell response to stiffness exhibits muscle-like behavior. *Proceedings of the National Academy of Sciences* **106**, 18243–18248 (2009).
43. Wang, H. *et al.* Necking and failure of constrained 3D microtissues induced by cellular tension. *Proc Natl Acad Sci U S A* **110**, 20923–20928 (2013).
44. Pakshir, P. *et al.* Dynamic fibroblast contractions attract remote macrophages in fibrillar collagen matrix. *Nat Commun* **10**, (2019).
45. Yeung, T. *et al.* Effects of substrate stiffness on cell morphology, cytoskeletal structure, and adhesion. *Cell Motil Cytoskeleton* **60**, 24–34 (2005).

46. Alisafaei, F., Jokhun, D. S., Shivashankar, G. V. & Shenoy, V. B. Regulation of nuclear architecture, mechanics, and nucleocytoplasmic shuttling of epigenetic factors by cell geometric constraints. *Proc Natl Acad Sci U S A* **116**, 13200–13209 (2019).
47. Kozlov, M. M. & Chernomordik, L. V. Membrane tension and membrane fusion. *Current Opinion in Structural Biology* vol. 33 61–67 Preprint at https://doi.org/10.1016/j.sbi.2015.07.010 (2015).
48. Lachowski, D. *et al.* Substrate Stiffness-Driven Membrane Tension Modulates Vesicular Trafficking via Caveolin-1. *ACS Nano* **16**, 4322–4337 (2022).
49. Guilak, F., Tedrow, J. R. & Burgkart, R. Viscoelastic Properties of the Cell Nucleus. *Biochem Biophys Res Commun* **269**, 781–786 (2000).
50. Vishavkarma, R. *et al.* Role of actin filaments in correlating nuclear shape and cell spreading. *PLoS One* **9**, (2014).
51. Lombardi, M. L. *et al.* The Interaction between Nesprins and Sun Proteins at the Nuclear Envelope Is Critical for Force Transmission between the Nucleus and Cytoskeleton*. *Journal of Biological Chemistry* **286**, 26743–26753 (2011).
52. Denisin, A. K., and Pruitt, B. L. Tuning the range of polyacrylamide gel stiffness for mechanobiology applications. ACS applied materials & interfaces **8**(34), 21893-21902 (2016).
53. Wang, H., S, A. A., Chen, C. S., Wells, R. G. & Shenoy, V. B. Long Range Force Transmission in Fibrous Matrices Enabled by Tension-Driven Alignment of Fibers. doi:10.1101/048579.
54. Zanotelli, M. R. *et al.* Regulation of ATP utilization during metastatic cell migration by collagen architecture. *Mol Biol Cell* **29**, 1–9 (2018).
55. Guo, M. *et al.* Cell volume change through water efflux impacts cell stiffness and stem cell fate. *Proceedings of the National Academy of Sciences* **114**, E8618–E8627 (2017).
56. Wang, W., Miller, J. P., Pannullo, S. C., Reinhart-King, C. A. & Bordeleau, F. Quantitative assessment of cell contractility using polarized light microscopy. *J Biophotonics* **11**, e201800008 (2018).
57. Hassan, S., Kim, J. & suo, Z. Polyacrylamide hydrogels. IV. Near-perfect elasticity and rate-dependent toughness. *J Mech Phys Solids* **158**, 104675 (2022).
58. Kosheleva, N. V *et al.* Building a tissue: Mesenchymal and epithelial cell spheroids mechanical properties at micro- and nanoscale. *Acta Biomater* **165**, 140–152 (2023).
59. Shi, Z., Graber, Z. T., Baumgart, T., Stone, H. A. & Cohen, A. E. Cell Membranes Resist Flow. *Cell* **175**, 1769-1779.e13 (2018).
60. Kim, D.-H. & Wirtz, D. Focal adhesion size uniquely predicts cell migration. *The FASEB Journal* **27**, 1351–1361 (2013).
61. Zimmerman, J. J., von Saint André-von Arnim, A. & McLaughlin, J. Chapter 74 - Cellular Respiration. in *Pediatric Critical Care (Fourth Edition)* (eds. Fuhrman, B. P. & Zimmerman, J. J.) 1058–1072 (Mosby, Saint Louis, 2011). doi:https://doi.org/10.1016/B978-0-323-07307-3.10074-6.
62. Lou, F., Curtin, N. A. & Woledge, R. C. The Energetic Cost of Activation of White Muscle Fibres from the Dogfish Scyliorhinus Canicula. *Journal of Experimental Biology* **200**, 495–501 (1997).
63. Crow, M. T. & Kushmerick, M. J. Correlated reduction of velocity of shortening and the rate of energy utilization in mouse fast-twitch muscle during a continuous tetanus. *Journal of General Physiology* **82**, 703–720 (1983).
64. Baker, A. J. *et al.* Energy use by contractile and noncontractile processes in skeletal muscle estimated by 31P-NMR. *American Journal of Physiology-Cell Physiology* **266**, C825–C831 (1994).

65. Hardie, D. G. AMP-activated protein kinase-an energy sensor that regulates all aspects of cell function. *Genes and Development* vol. 25 1895–1908 Preprint at https://doi.org/10.1101/gad.17420111 (2011).
66. Derricks, K. E., Trinkaus-Randall, V. & Nugent, M. A. Extracellular matrix stiffness modulates VEGF calcium signaling in endothelial cells: individual cell and population analysis. *Integrative Biology* **7**, 1011–1025 (2015).
67. Wicher, S. A. *et al.* Aging increases senescence, calcium signaling, and extracellular matrix deposition in human airway smooth muscle. *PLoS One* **16**, (2021).
68. Kim, T. J. *et al.* Substrate rigidity regulates Ca2+ oscillation via RhoA pathway in stem cells. *J Cell Physiol* **218**, 285–293 (2009).
69. Luo, M. *et al.* Compression enhances invasive phenotype and matrix degradation of breast Cancer cells via Piezo1 activation. *BMC Mol Cell Biol* **23**, (2022).
70. Kim, T. J., Sun, J., Lu, S., Qi, Y. X. & Wang, Y. Prolonged mechanical stretch initiates intracellular calcium oscillations in human mesenchymal stem cells. *PLoS One* **9**, (2014).
71. Mcgee, S. L. & Hargreaves, M. *AMPK and Transcriptional Regulation*. *Frontiers in Bioscience* vol. 13 (2008).
72. Richter, R. P. *et al.* Glycocalyx heparan sulfate cleavage promotes endothelial cell angiopoietin-2 expression by impairing shear stress-related AMPK/FoxO1 signaling. (2022) doi:10.1172/jci.
73. Lo, C.-M., Wang, H.-B., Dembo, M. & Wang, Y.-L. *Cell Movement Is Guided by the Rigidity of the Substrate*. (2000).
74. Khetan, S. *et al.* Degradation-mediated cellular traction directs stem cell fate in covalently crosslinked three-dimensional hydrogels. *Nat Mater* **12**, (2013).
75. Cóndor, M. *et al.* Breast Cancer Cells Adapt Contractile Forces to Overcome Steric Hindrance. *Biophys J* **116**, 1305–1312 (2019).
76. Graham, D. M. *et al.* Enucleated cells reveal differential roles of the nucleus in cell migration, polarity, and mechanotransduction. *Journal of Cell Biology* **217**, 895–914 (2018).
77. Han, Y. L. *et al.* Cell contraction induces long-ranged stress stiffening in the extracellular matrix. *Proc Natl Acad Sci U S A* **115**, 4075–4080 (2018).
78. Godbout, C. *et al.* The Mechanical Environment Modulates Intracellular Calcium Oscillation Activities of Myofibroblasts. *PLoS One* **8**, e64560- (2013).